CHALMERS

Deposition and Characterization of Dielectric Distributed Bragg Reflectors

MICHAEL LAPP

Erasmus Mundus Master of Science in Nanoscience and Nanotechnology

Promoter: Prof. Anders Larsson
Co-promoter: Prof. Kristiaan Temst

KU LEUVEN

Department of Microtechnology and Nanoscience
CHALMERS UNIVERSITY OF TECHNOLOGY
Gothenburg, Sweden 2016

Funded by the
Erasmus+ Programme
of the European Union

MASTER'S THESIS IN ERASMUS MUNDUS MASTER OF SCIENCE IN NANOSCIENCE AND NANOTECHNOLOGY

Deposition and Characterization of Dielectric Distributed Bragg Reflectors

MICHAEL LAPP

Department of Microtechnology and Nanoscience
Photonics Laboratory
CHALMERS UNIVERSITY OF TECHNOLOGY
Gothenburg, Sweden 2016

Deposition and Characterization of Dielectric Distributed Bragg Reflectors
MICHAEL LAPP

ISSN 1652-8557
Department of Microtechnology and Nanoscience
Photonics Laboratory
Chalmers University of Technology
SE-412 96 Gothenburg
Sweden
Telephone: +46 (0)31-772 1000

Chalmers Reproservice
Gothenburg, Sweden 2016

Deposition and Characterization of Dielectric Distributed Bragg Reflectors
Master's thesis in Erasmus Mundus Master of Science in Nanoscience and Nanotechnology
MICHAEL LAPP
Department of Microtechnology and Nanoscience
Photonics Laboratory
Chalmers University of Technology

Abstract

The Vertical Cavity Surface Emitting Laser (VCSEL) is a laser well suited for data centre applications due to its low cost, high speeds, good fiber coupling, and low threshold current The current standard wavelength for short-haul is 850 nm, however switching to 980 nm can improve transmission distance in optical fiber by lowering absorption and chromatic dispersion. To improve the performance of VCSELs, mirrors with less optical loss can be used. VCSELs require mirrors with $>99\,\%$ reflectance, and Distributed Bragg Reflectors (DBRs) are used to achieve this. Today, epitaxially-grown semiconductor DBRs are used, however these have low refractive index contrast, scattering from dopants, and free-carrier absorption. These DBRs can be replaced by dielectric ones which can offer higher refractive index contrast and less absorption. These properties can increase optical confinement in the gain region and decrease losses in the mirrors leading to VCSELs with more output power and lower threshold currents. DBRs using dielectric materials to reflect 980 nm light above 99 % are therefore of key interest.

In this work DBRs with SiO_2/TiO_2 layers as well as SiO_2/a-Si were deposited by sputtering. Mirrors were fabricated with 2, 4, 6, and 8 pairs for each set of materials. A measurement setup was built to measure reflectances above 99 % with $\pm 0.03\,\%$ accuracy to evaluate the mirrors.

DBRs of SiO_2/TiO_2 were found to achieve above 99 % reflectance for 6 and 8 pairs with measured reflectances of $99.42 \pm 0.03\,\%$ and $99.80 \pm 0.03\,\%$ respectively with negligible extinction coefficient. SiO_2/a-Si DBRs achieved over 99 % reflectance for 4, 6, and 8 pairs with measured reflectances of $99.36 \pm 0.03\,\%$, $99.02 \pm 0.03\,\%$, and $99.17 \pm 0.03\,\%$ respectively with extinction coefficient for a-Si between 0.0010 and 0.0015 at 980 nm. All DBRs agreed well with simulated results.

SiO_2/TiO_2 mirrors were found to have more reliable deposition and achieved higher reflectances. SiO_2/a-Si DBRs on the other hand were found to have less reliable deposition and their reflectance saturated above 6 pairs due to the higher extinction coefficient in a-Si, indicating little to no light is transmitted out of these DBRs, limiting their usefulness for VCSELs.

A 6-pair SiO_2/TiO_2 DBR appears very promising to use in VCSELs due to the superior reliability of the materials and increased output power from a slightly lower reflectance than the 8-pair mirror.

Keywords: Vertical Cavity Surface Emitting Laser (VCSEL), Distributed Bragg Reflector (DBR), z-method, SiO_2, TiO_2, a-Si, dielectrics, thin-films, sputtering, ellipsometry, reflectance, 980 nm

Acknowledgements

First and foremost I would like thank my supervisor Emanuel Haglund and examiner Professor Anders Larsson for the opportunity to work on this project, and a warm welcome into the Photonics Lab. Especially to Emanuel, for many fruitful discussions and always having an open door to answer my questions. In addition, I would like to express my gratitude to the cleanroom staff for the many trainings and prompt service, specifically to Henrik Frederiksen for his patience despite my penchant for running into problems with the sputtering tool.

A shout-out to my friends and family back home! And to the new friends I have made from all over the globe while studying in Belgium and Sweden over the past 2 years. Never a dull moment.

And finally, my deepest thanks to my parents Terry and Jonathan, and sister Katie, for giving me the courage and support to step out of my comfort zone and pursue this degree across the pond. It was the best decision I've ever made.

It's been a slice,
Michael

Göteborg, June 2016

Contents

Chapter 1

Introduction

Today's information society was enabled by advances in telecommunications, and further advances are always needed to meet society's demand for more connectivity. This creates a positive feedback where networks need to improve to scale with the demands put on them, and by improving, the demands are then pushed further. More people and devices are connected now than ever, and this trend shows no sign of stopping where today everything from phones to cars to refrigerators are connected to the Internet. More and more devices are acting as terminals, accessing more powerful computational resources located elsewhere. This is commonly referred to as cloud-computing where the processing and storage of data is done in large data centres. These data centres are internally connected with millions of short-haul optical links, and connected to other data centres and larger networks through long-haul links to send the processed data over continents and across oceans. Electricity costs are one of the dominating operating expenses for data centres, and are expected to surpass the cost of initial investment of building data centres [1].

1.1 Motivation

By improving the operation of lasers used in telecommunication networks, higher speeds, further reach, and lower power consumption can be achieved. These factors have significant economical impacts for network operators. In data centres, the main criteria for choosing a laser are low cost, low power consumption, and high speeds. Reach is not a significant criteria here since links are short within data centres. An important type of laser for data centres is the Vertical Cavity Surface Emitting Laser (VCSEL), where the resonance cavity is vertical (compared to the horizontal substrate), and light is emitted from the surface of the device. VCSELs offer low production cost, low power consumption, and rates exceeding 50 Gb/s [2] [3]. Improving the operation of VCSELs is therefore of prime importance, and one way to do this is to lower the optical loss in the mirrors. Lower optical loss means more reflectance in the mirrors, as well as more output power for the same input power into the laser. One path to achieve this is to replace one or both of the semiconductor Distributed Bragg Reflectors (DBRs) in a VCSEL with dielectric ones. A DBR is a stack of layers with alternating refractive index configured such that they can achieve very high reflectances at a particular wavelength. On top of lower

optical loss, dielectric DBRs can have more reflectivity at each interface, pushing more of the electromagnetic field into the active region of the laser where gain occurs. Thus dielectric DBRs can lower the optical loss and improve confinement to the gain region of VCSELs [4].

980 nm lasers are of particular interest since they are widely deployed in existing telecommunications networks for long-haul communication [5] [6]. They are used extensively in Erbium Doped Fiber Amplifiers (EDFAs) which allow all optical amplification in links without the need to convert the signal from optical to electrical, amplify, and then convert it back to optical [7]. Improved 980 nm lasers will allow lasers driven with less power to pump EDFAs, reducing power consumption. VCSELs are unlikely to replace existing 980 nm lasers for this application in the near future since their output power is too low, however with continued advances it could become feasible in the future.

More importantly, 980 nm is being looked at for short-haul transmission, within data centres in particular [8]. The current standard wavelength for short-haul is 850 nm, but switching to 980 nm offers some advantages [9], e.g. the optical fiber has less absorption and less chromatic dispersion at 980 nm compared to 850 nm. This allows less power to drive the lasers over the same transmission distance, or for the same power the transmitted data can travel error-free for longer distances. Lower power at the receiver can also have a ripple effect, allowing simpler receiver designs that also use less energy.

Improved VCSELs operating at 980 nm through the use of dielectric DBRs can have a significant positive impact on optical communication for both short- and long-haul applications.

1.2 Goals of Thesis

The main goal of this thesis is to study the impact of material choice and number of pairs on the reflectance of dielectric DBRs designed to reflect light at 980 nm. This will be done by simulations, as well as measurements on DBRs fabricated with sputtering. Using DBRs in VCSELs requires a reflectance >99%, which places a secondary goal on this thesis of building and analyzing a measurement setup able to measure the absolute reflectance with sufficient precision to properly analyze the fabricated DBRs. The results of this work will be used in the future to make VCSELs at 980 nm integrating a dielectric DBR to the current fabrication processes. In addition, a more precise measurement technique will be available to test reflectance than existed at the onset of this Master's thesis.

The work to be done on this thesis is:

- Build precise measurement setup
- Fabricate DBRs
- Develop simulations
- Characterize DBRs
- Analyze results

1.3 Outline of Thesis

The thesis is divided into Chapters as follows: Chapter 1 provides context and motivation for the work undertaken, and Chapter 2 introduces the operation of semiconductor lasers, in particular VCSELs and DBRs. Following this, Chapter 3 presents the experimental techniques used to fabricate and characterize DBRs. In Chapter 4, the material requirements for VCSEL DBRs are given and the advantages of using dielectric materials are presented with a motivation for the choices of particular dieletrics. In Chapter 5, the results are presented and discussed. This includes how well the reflectance measurement setup works, along with a comparision of the measured reflectances for DBRs deposited with different materials and number of pairs, accompanied by simulated results. Finally, the conclusions of the thesis are given in Chapter 6.

Chapter 2

Static Operation of VCSELs

Laser is an acronym for Light Amplification by Stimulated Emission of Radiation. To amplify the light, a gain medium is required where an incident photon can stimulate the emission of an identical photon (same wavelength, phase, direction) by de-exciting an electron from a high energy state to a lower energy state where the energy difference is the same as the energy of the incident photon. To enhance the amplification, the gain medium is placed in a resonator consisting of two mirrors with the gain medium in between. This way photons will continually pass through the gain medium causing further amplification. To achieve output light, one of the mirrors must be semi-transparent. To ensure there is population inversion in the gain material, pumping must be used to continuously place electrons in the required higher energy level. To achieve lasing, the gain must be high enough to compensate all losses, and the phase must repeat itself in the resonator to achieve coherent light output.

The threshold material gain, g_{th}, is the minimum gain needed to overcome losses for lasing and is given by

$$g_{th} = \frac{1}{\Gamma}[\alpha_i + \alpha_m] = \frac{1}{\Gamma}\left[\alpha_i + \frac{1}{2L}\ln\frac{1}{R_1 R_2}\right], \tag{2.1}$$

where Γ is the optical confinement factor (the overlap between the active region and the optical field), α_i is the internal loss, α_m is the mirror loss, L is the cavity length, and R_1 and R_2 are the power reflectances of the mirrors [10].

The phase condition for lasing requires that the phase of the field must be repeated after one round trip, and is given by

$$\exp\left(-j\frac{2\pi}{\lambda_0/n_{eff}}2L\right) = 1 \implies \lambda_0 = \frac{2Ln_{eff}}{m}, \tag{2.2}$$

where λ_0 is the lasing wavelength, n_{eff} is the effective refractive index of the active region, and m is an integer. Lasing at a certain wavelength will only occur when both the threshold gain and cavity resonance requirements are met for that wavelength [10].

The first laser was demonstrated in 1960 by Maiman [11], and was followed by the first semiconductor laser demonstrated by Hall et. al. in 1962 [12]. The VCSEL was first suggested by Iga in 1977 [13], and demonstrated 2 years later in 1979 by Iga's group [14].

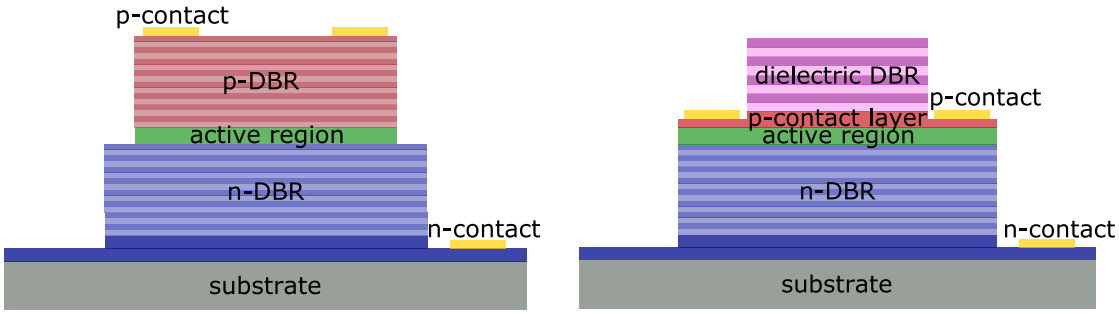

(a) (b)

Figure 2.1: *Schematic cross-sections for (a) standard VCSEL and (b) VCSEL with dielectric top DBR*

2.1 Semiconductor Lasers

The active region in a semiconductor laser typically consists of a forward biased *pin*-junction. The *p*- and *n*-doped regions consist of semiconductors with higher band gap than the intrinsic gain material sandwiched between. This allows population inversion to occur with electrical pumping where electrons will accumulate in the conduction band of the lower bandgap gain material [10] [15]. These electrons can then be stimulated by photons to create amplification. When enough electrons accumulate to overcome the losses, lasing will occur. This is defined by the threshold current, I_{th}.

The simplest semiconductor laser is the Fabry-Perot laser where the mirrors are formed from cleaving the substrate, creating air/semiconductor interfaces. The configuration of these lasers allows the optical field to interact with the gain region over a large distance, so the relatively low reflectance of the air/semiconductor interface provides sufficient reflectance to meet the gain threshold. This type of laser is called an edge-emitter since light is output from the edges of the device.

2.2 Vertical Cavity Suface Emitting Laser

VCSELs employ a cavity perpendicular to the substrate surface as opposed to edge-emitters where the cavity is parallel to the substrate surface. By using a perpendicular cavity, light is then also output perpendicular to the substrate surface. This is a huge advantage over edge-emitters for large scale manufacturing since wafer-level testing can be performed, whereas only device-level testing can be done for edge-emitters where the wafer must be diced before testing [10]. The drawback to vertical cavities is that the length over which the light can interact with the active region is very small, resulting in a small optical confinement factor. As a result, in order to meet the threshold gain requirement, mirrors with reflectances in excess of 99% are required [15]. To achieve such large reflectances, a special type of mirror called a Distributed Bragg Reflector (DBR) is used. The theory of DBRs is outlined in Section 2.2.1. A cross-section of a typical VCSEL is shown in Figure 2.1a.

The active region for 980 nm VCSELs typically consists of multiple strained $In_xGa_{1-x}As$ quantum wells. The epitaxial DBRs must be lattice matched to the quantum wells, and typically employ doped $GaAs/Al_xGa_{1-x}As$ layers. This limits the refractive index contrast, and requires DBR stacks in excess of 20 layers [16] [17]. Dielectric materials on the other hand can yield much higher refractive index contrasts, so dielectric DBRs can require less than 10 pairs to achieve the required reflectance.

Semiconductors are able to conduct heat away from the active region through the bottom DBR to the substrate. This is important because if too much heat accumulates, the VCSELs output power will drop. This is in contrast to dielectrics which are not thermally conductive, so they are a poor choice for bottom DBR, but for a top DBR they are fine. As a result VCSELs where the top reflector is a dielectric DBR while the bottom is semiconductor DBR are of interest, shown in Figure 2.1b. VCSELs with a bottom dielectric DBR, or both mirrors as dielectrics are still feasible, but more processing steps need to be done to remove heat from the cavity to maintain the VCSELs performance [18] [19]. Some techniques are being explored to mitigate this such as adding heat spreading layers [19].

2.2.1 Distributed Bragg Reflectors

The Fresnel equations govern how light behaves at the interface of two materials [20]. For the case of DBRs used in VCSELs, only light incident perpendicular to the surface is of interest, simplifying the equations since polarization no longer matters at normal incidence. The amplitude reflection coefficient, r, going from material 1 to material 2 is then given by

$$r = \frac{E_{0r}}{E_{0i}} = \frac{n_2 - n_1}{n_1 + n_2}, \tag{2.3}$$

where E_{0r} and E_{0i} are the amplitudes of the reflected and incident electric fields respectively, and n_1 and n_2 are the refractive indices of material 1 and 2 respectively. What is of more use than r is the reflectance, R, defined as the ratio of the reflected power to the incident power

$$R \equiv \frac{E_{0r}^2}{E_{0i}^2} = r^2 = \left[\frac{n_2 - n_1}{n_1 + n_2}\right]^2. \tag{2.4}$$

From Equation 2.4 it is seen that a larger contrast in refractive index gives a larger reflectance. For example a glass window with $n_{air} = 1$ and $n_{glass} = 1.5$ gives $R = 4\,\%$. Whereas for materials with a higher refractive index contrast with $n_1 = 1$ and $n_2 = 2.5$ gives $R = 18\,\%$.

Equation 2.3 also gives information about phase changes at the material interface. For $n_2 > n_1$, r will be positive which indicates the electric field of the reflected wave is in phase with the electric field of the incident wave. For this to occur, a π-phase shift must occur at the boundary. For the case $n_1 > n_2$, r will be negative meaning the reflected wave is out of phase with the incident wave and no phase shift occurs at the interface.

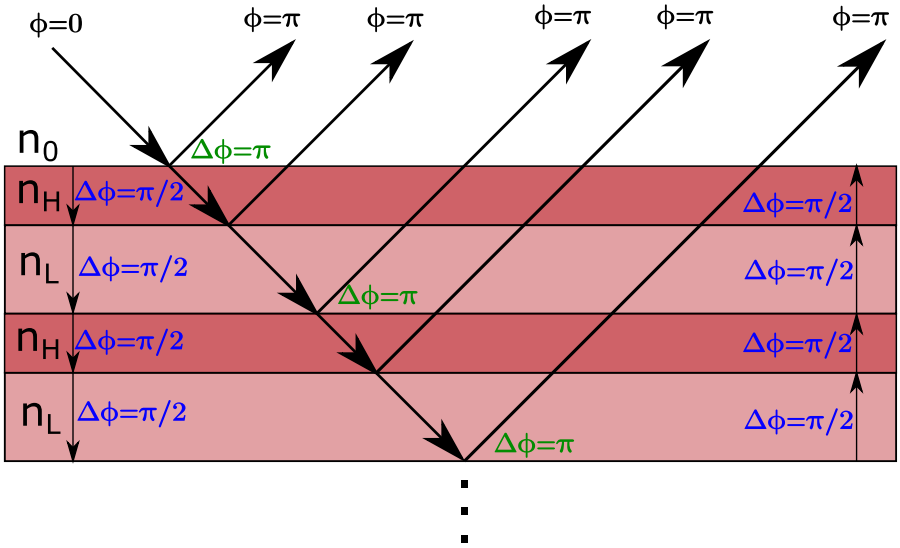

Figure 2.2: *Schematic cross-section of DBR with light incident from air. In blue are phase changes due to propagating a layer, in green are phase changes due to reflections, and in black is the overall phase of light leaving the surface. In reality light is incident perpendicular to the surface, but is shown here at an angle for illustration.*

For conservation to occur, $t + r = 1$ where t is the amplitude transmission coefficient of the incident electric field into the second material. Using this with the last part of Equation 2.3 gives

$$t = \frac{2n_1}{n_1 + n_2}. \tag{2.5}$$

From Equation 2.5, it is seen that t will always be positive, so no phase shift occurs for transmitted light.

The results for reflection and phase change at interfaces can be exploited to create a mirror with large reflectance. To get more reflectance, alternating layers of high and low refractive index materials can be stacked. The more layers that are added, the higher the resulting reflectance will be. In addition, the reflections should all be in phase with each other to get constructive interference. To achieve constructive interference, layers with thicknesses of $\lambda/4$ can be used (where λ is the wavelength inside the material). A schematic of a DBR can be seen in Figure 2.2.

This way, for every layer the light propagates into the stack, it must travel back to the surface for reflection, meaning it travels a distance of $\lambda/2$ per layer which results in a phase shift of π. If the light travels an odd number of layers before reflection, the total phase shift will be π, while for an even number of layers there will be no phase shift. If the top layer is a high index material, then after travelling an odd number of layers, the reflection will be from high to low, so no phase shift will occur resulting in an overall π-phase shift for an odd number of layers. For an even number of layers, the reflection occurs at a low-to-high interface, so a

π-phase change will occur, combined with no phase shift for travelling through an even number of layers resulting in a reflection at the surface with a π-phase shift. Of course light can be reflected multiple times within the DBR, however with these conditions all light leaving the top surface will have a π-phase change. This way all reflections will leave the surface with the same phase (π-phase shift with respect to the incident field) [21].

Transfer Matrix Method for DBRs

To calculate the reflectance of a DBR, a transfer matrix method may be employed where the interfaces and propagation through layers are modelled with a transmission matrix. Multiplying the matrices together in the correct order yields the overall transfer matrix of the DBR. From the transfer matrix, the reflectance of the DBR can be calculated.

We assume TE-polarized electromagnetic waves at normal incidence with forward and backward propagation given by

$$E = a_1 e^{ikx} + b_1 e^{-ikx}, \tag{2.6}$$

where a_1 and b_1 are the amplitudes of the forward and backward propagating waves respectively, x is the position, and k is the wavenumber given by $\frac{2\pi}{\lambda}$. The transfer matrix method allows you to study the transmission through a system relating electromagnetic waves at one side to the other by

$$\begin{bmatrix} a_1 \\ b_1 \end{bmatrix} = \mathbf{M} \begin{bmatrix} a_2 \\ b_2 \end{bmatrix}, \tag{2.7}$$

where $\mathbf{M}$ is the transfer matrix of the entire system. The transfer matrix is made up by multiplying the individual transfer matrices of each component in the system together. The system is made of two components, interfaces and propagation [22]. The interface transfer matrix for incidence from material 1 to material 2 is given by

$$\mathbf{I_{12}} = \frac{1}{t_{12}} \begin{bmatrix} 1 & r_{12} \\ r_{12} & 1 \end{bmatrix}, \tag{2.8}$$

where t_{12} is the transmission amplitude coefficient from material 1 to material 2 and r_{12} is the reflection amplitude coefficient.

The transfer matrix for propagation through a material is

$$\mathbf{P_1} = \begin{bmatrix} e^{i(n_1 + i\kappa_1)kd_1} & 0 \\ 0 & e^{-i(n_1 + i\kappa_1)kd_1} \end{bmatrix}, \tag{2.9}$$

where n_1 is the refractive index, κ_1 is the extinction coefficient, and d_1 is the width of the material. If κ_1 is non-zero, there will be some exponential decay while propagating through the layer. We now have all of the tools necessary to develop the overall transfer matrix for transmission through a DBR. We will go through the technique for the DBR shown in Figure 2.3.

Here we have light incident from air onto a 2-pair DBR on a substrate. We will set the coefficient b_2 to zero since we have light incident from air, and no light incident from the

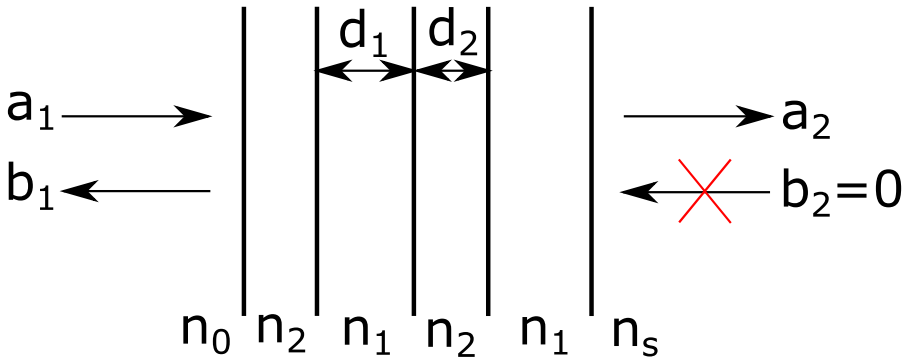

Figure 2.3: *Alternating material stack with light incident from the left, a transmitted component leaving the stack on the right, and a reflected component leaving the stack on the left. There is no incidence from the right.*

substrate. The full transmission transfer matrix multiplication through each component in this stack is given by

$$\begin{bmatrix} a_1 \\ b_1 \end{bmatrix} = \mathbf{I_{02}P_2I_{21}P_1I_{12}P_2I_{21}P_1I_{1s}} \begin{bmatrix} a_2 \\ 0 \end{bmatrix}. \tag{2.10}$$

To simplify this for DBRs, we can break up $\mathbf{I_{ij}}$ into an equivalent representation of

$$\mathbf{I_{ij}} = \mathbf{I_i^{-1}I_j} = \begin{bmatrix} 1 & 1 \\ n_i & -n_i \end{bmatrix}^{-1} \begin{bmatrix} 1 & 1 \\ n_j & -n_j \end{bmatrix}, \tag{2.11}$$

to give

$$\begin{bmatrix} a_1 \\ b_1 \end{bmatrix} = \mathbf{I_0^{-1}}(\mathbf{M_{DBR}})^{\mathbf{N}}\mathbf{I_s} \begin{bmatrix} a_2 \\ 0 \end{bmatrix}, \tag{2.12}$$

where $\mathbf{M_{DBR}}$ is the transfer matrix of one DBR pair given by $\mathbf{M_{DBR}} = \mathbf{I_2P_2I_2^{-1}I_1P_1I_1^{-1}}$, and N is the number of pairs in the DBR. This represenation is particularly useful for programming simulations of DBR stacks. Now the total transfer matrix is given by

$$\begin{bmatrix} a_1 \\ b_1 \end{bmatrix} = \mathbf{M} \begin{bmatrix} a_2 \\ 0 \end{bmatrix} = \begin{bmatrix} M_{11} & M_{12} \\ M_{21} & M_{22} \end{bmatrix} \begin{bmatrix} a_2 \\ 0 \end{bmatrix}. \tag{2.13}$$

Now the reflectance can be computed as

$$R = r^2 = \left(\frac{b_1}{a_1}\right)^2 = \left(\frac{M_{21}a_2}{M_{11}a_2}\right)^2 = \left(\frac{M_{21}}{M_{11}}\right)^2, \tag{2.14}$$

where a_2 conveniently cancels out.

Chapter 3

Experimental Techniques

This chapter explains the experimental methods and techniques used is this thesis. It includes the tools used to process the DBRs in the cleanroom, techniques used to characterize the films, and the experiments performed to measure the reflectance of the deposited DBRs. The techniques are presented in roughly the order they were used to fabricate and test each reflector.

3.1 Sputtering

Sputtering is a method to deposit thin films on a substrate. This section provides an introduction to the tool used and its capabilities along with a basic overview of the operating principles. Finally, a description of the deposition parameters and how they influence the deposited films is presented.

3.1.1 Operating Principle

Sputtering is a process where energetic particles are used to bombard a target. The high energy particles are able to overcome the binding energy of the particles in the target, and as a result particles of the target material are ejected. The ejected particles will coat any surface in their path. By placing a substrate in the path of the particles, a thin film of the target will be formed on the substrate [23]. A typical sputtering setup is shown in Figure 3.1

The tool used in this work was the FHR MS150. The high energy sputtering particles are provided by a plasma of argon in this tool. Argon is chosen since it is a noble gas, and will not react with the target particles or substrate. Argon is cheap and abundant, and has an atomic mass close to that of the materials to be used in this thesis which provides more efficient sputtering.

The tool makes use of magnetron sputtering, which is a technique employed to speed up the sputtering process. This works by using a magnetron to shape strong electromagnetic fields near the surface of the target. This keeps the plasma closer to the target, and ionizes more argon particles due to accelerating electrons in the magnetron's field. These two factors increase the number of sputtering events, and therefore decrease the deposition time. The

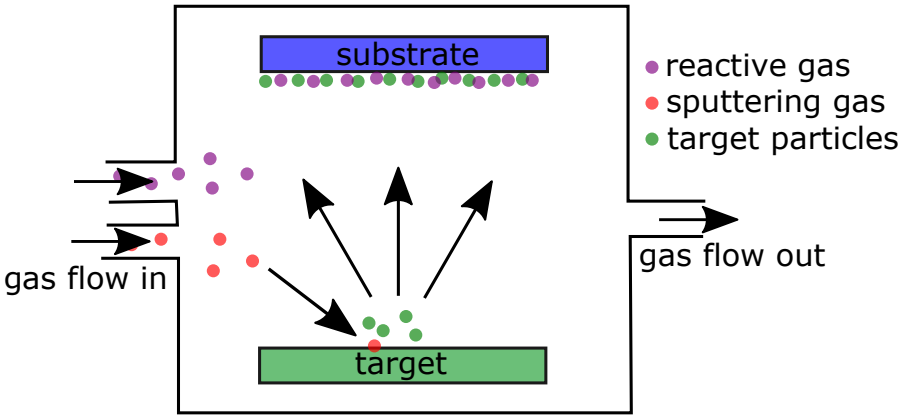

Figure 3.1: *Diagram of reactive sputtering chamber for thin-film deposition.*

sputtered particles are neutral, so they are not trapped by the magnetron and are free to coat the substrate [23].

There are different sputtering processes depending on the target used and the thin-film to be deposited. The tool is capable of both DC and RF sputtering. For conducting targets, DC sputtering is used where the target has a DC bias. Since the target is conductive, there is no accumulation of charges on the surface of the target. DC allows a cheaper power source to be used. However, for insulating targets, DC sputtering is not an option since charge will build up on the surface and can form arcs. As a result, RF sputtering is used instead where the substrate bias is alternated. This allows the charged argon to sputter for a half cycle, then the charges are removed from the surface for the next half cycle. This way no charge is accumulated on the target surface [23].

Thin films of compound materials can be deposited with this tool using reactive sputtering. Reactive sputtering involves an additional flow of a reactive gas into the sputtering chamber. The sputtered particles and the reactive gas combine to create films of compound materials. For example, to deposit a thin film of SiO_2, a target of pure silicon is used along with a gas flow of O_2. The silicon and oxygen react to form a SiO_2 film [23]. The tool has the capability of using O_2 and N_2 as reactive gases. One thing to note for the tool is that nitrogen and oxygen gases share the same pipes. As a result, when switching between the two gases for reactive sputtering, the pipes must be flushed first to ensure no contamination from the other gas. This is a time-consuming process and drastically increases the deposition time.

3.1.2 Deposition Parameters

There are a number of deposition parameters that can be controlled by the tool, and each parameter will influence the properties of the sputtered film on the substrate.

One parameter is the power applied to the plasma. For higher power, the argon ions will have more energy when they hit the target, allowing more target particles to be sputtered per collision. This will decrease the depostion time needed. In addition, the higher energy collisions

will provide more energy to the sputtered particles. This means the deposited films will be denser [23].

In addition, the pressure in the chamber can be controlled. The pressure influences how the sputtered particles travel through the chamber to the substrate. Under low pressure, the sputtered particles will travel ballistically to the substrate since there are few particles in the chamber to collide with. This means the sputtered particles will have more energy under low pressure, leading to denser films. Under higher pressures, the sputtered particles will travel diffusively to the substrate since more collisions will take place. This lowers the energy of the sputtered particles, creating less dense films [23].

In reactive sputtering, the mass flow of the reactive gas into the chamber will influence the film deposition. The flow will influence where the reaction of the reactive gas with the target material will take place, at the surface of the target, in the chamber, or at the surface of the substrate. In addition, the mass flow can influence the stoichiometry of the resulting film [23].

The thickness of the film is mainly controlled by the deposition time. When the other parameters have been set and controlled, a certain deposition rate will be obtained onto the substrate. By knowing this rate, one can set the deposition time to get a film of the required thickness.

The tool is also able to bias the substrate. This can help make denser films, and ensure all the films are bonded well, however it can also lead to re-sputtering. Re-sputtering is when argon ions collide with the substrate, and sputter substrate particles away. Substrate bias was not used in this thesis since re-sputtering could lead to more roughness at the surface of the thin-films.

Standard recipes have been developed for the various materials that can be sputtered to yield reliable films. For the most part these standard recipes have been used in this thesis. It is important that all of these parameters are well controlled to achieve flat films since it has been shown that surface roughness of >1nm can have a negative impact on the reflectance of DBRs [24]. Films will be deposited on 2" silicon wafers. Silicon wafers are chosen since they are less expensive than other wafers, e.g. GaAs.

3.2 Ellipsometry

Ellipsometry is a technique used to determine the complex refractive index and thickness of thin-films. It operates by having incident radiation at a known wavelength, angle of incidence, and polarization state onto a sample. The polarization change is measured after interacting with the sample. A basic setup of an ellipsometer can be seen in Figure 3.2.

The polarization change is measured by the complex reflectance ratio, ρ, which is given by

$$\rho = \frac{r_p}{r_s} = \tan\Psi e^{i\Delta}, \tag{3.1}$$

where r_p and r_s are the amplitudes of the s- (perpendicular) and p- (parallel) polarization components after reflection, and normalized to their initial values. To achieve the best resolution, an angle close to the Brewster angle (where $r_p = 0$) should be chosen to maximize contrast in

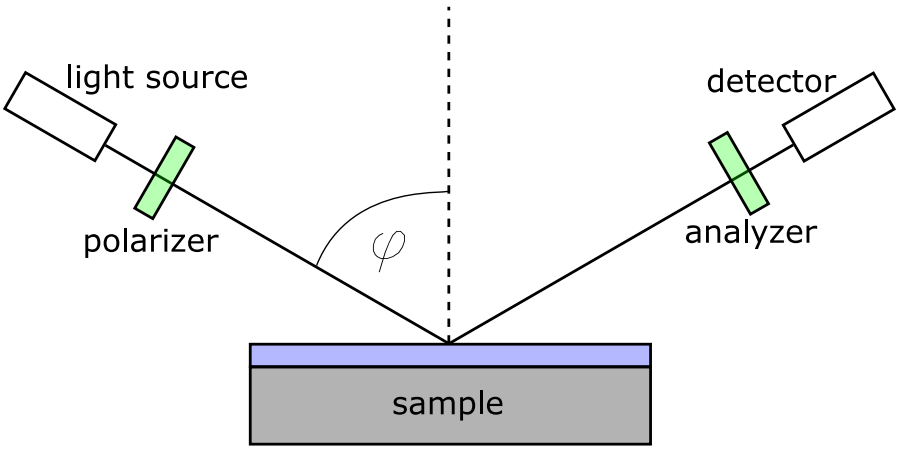

Figure 3.2: *Schematic of typical ellipsometer setup.*

r_p and r_s. An alternative representation is provided where $\tan\Psi$ is the amplitude ratio after reflection and Δ is the phase shift after reflection [23].

Some advantages to this method are that it is able to determine layer thicknesses less than the incident wavelength, it is non-destructive for the samples, and since it measures a ratio, it is insensitive to fluctuations and requires no reference sample. However, it is not a direct measurement method for thickness or complex refractive index. Instead it relies on building a model [23].

A model of the structure under test is built starting with the substrate at the bottom, and adding the thin-film layers on top to simulate what is being tested. For a silicon substrate, the complex refractive index distribution is well known, and since the the substrate is a bulk material, its precise thickness is not required to achieve good results. For the other layers, it is important to provide reasonable starting values for the layer thickness and complex index of refraction to ensure the parameters will be able to converge to the best solution [25].

Once the model is built, data is generated of how light should propagate through the stack for the given wavelength, angle of incidence, and polarization. The fitting parameters are then altered to get the simulated data as close as possible to what was measured. If the starting parameters are too far off from the actual ones, the fitting can get stuck in a local minimum, and will not converge to the global minimum which is where the true values should lie. Each layer of the stack uses a different model depending on the material composition.

The models can be based on a dispersion relation for the index of refraction and extinction coefficient, or on tabulated experimental data. Typically, tabulated experimental data is used for layers where the optical properties are well known, e.g. a crystalline silicon substrate or thermally oxidized SiO_2. The tabulated data comes from published results. Dispersion models are more useful where the process to make the layer is less controlled, and is therefore needed for sputtered films since the layers will not be as uniform [25]. Some of these models are described in Sections 3.2.1 and 3.2.2.

3.2.1 Cauchy Model

For many materials, in particular dielectrics, n and κ can be modelled as a slowly varying function of λ and an exponential absorption tail respectively given by

$$n = A + \frac{B}{\lambda^2} + \frac{C}{\lambda^4}, \tag{3.2}$$

$$\kappa = \alpha \exp\left(1.24\beta\left(\frac{1}{\lambda} - \frac{1}{\gamma}\right)\right), \tag{3.3}$$

where A, B, C, α, and β are fitting parameters and γ is the band edge. λ and γ are in units of microns. Equation 3.3 corresponds to Urbach absorption which was proposed by Urbach as an empirical formula [26], and later given a theoretical basis for amorphous dielectrics below the band edge [27]. This model is therefore valid for materials with low extinction coefficient and slowly changing refractive index below the band edge of the material.

3.2.2 Oscillator Models

If the material does not meet the criteria for using the Cauchy model, then a general oscillator model can be used instead. These are more complicated models with more fitting parameters, but are able to account for large changes in n and κ. In addition, they are not limited to a specific region since they are more general [25].

3.2.3 Point-by-Point Fit

In addition to using equations like the Cauchy and oscillator methods, the fitting parameters n and κ can be determined using a point-by-point method where the measured data at a given wavelength, n and κ will be empirically fit to yield the closest result to the collected data. This method typically uses another model first to get the layer thickness correct and the other parameters close. Then you can do the point-by-point method. One drawback of this method compared to the others is that it does not ensure the values are consistent with the Kramers-Kronig relation. This means it is possible to get values that are not physically possible [25].

3.2.4 Typical Fitting Process

Using a Cauchy layer, the fit is first done for only film thickness (with the expected thickness as a starting point) since this tends to have the largest impact on the fit. Next, the coefficients A, B, and C are fit to get an estimate of n along with fitting for film thickness. Finally, the remaining parameters are fit along with the previous ones to get overall results for thickness, n, and κ. κ is fit last since the absorption of the dielectrics used is low, so it will have the least impact on the fit. Depending on the material used and the location of its band edge, the fit can be restricted to only certain wavelengths. This is useful since Urbach absorption is only valid for below the band edge.

3.2.5 Measurements

All measurements were performed in the cleanroom using a Woollam M2000 ellipsometer. Prior to each measurement, the sample is aligned to ensure the detector receives the most light possible. Also, the polarizer for incident light is set to 45°, corresponding to circularly polarized light where the s- and p-components are equal. For each measurement, the full spectral range available of 250-1000 nm was used. In addition, each measurement was done at incident angles of 65°, 70°, and 75°. By using more incident angles, more data is available for the fitting procedure, leading to more accurate fits.

3.3 Surface Profiler

A surface profiler is a tool used to gain information about surface topography with a vertical resolution on the nanoscale. The tool used in this work was a KLA-Tencor P-15 Profiler. This tool uses contact mode, where a diamond stylus is vertically placed in contact with the wafer, and then the wafer is moved laterally with the stylus always in contact. The height of the stylus is recorded at each step to get the overall surface topography [23]. The tool is useful for many applications, for example to obtain the step height of a nanoscale feature on the surface of a wafer. In this work, it was used to compute the stress of dielectric thin-film stacks.

To compute stress, two measurements are required, one before depositing any films to get the initial surface topography, and one following the deposition. The height of the surface, $y(x)$, is calculated from a polynomial fit to the measured data where the initial surface topography has been subtracted from the topography after deposition. The radius of curvature, R, can then be calculated with [28]

$$R = \frac{[1 + (dy/dx)^2]^{3/2}}{d^2y/dx^2}. \tag{3.4}$$

The radius of curvature measures how much bowing is present following the deposition. With R, the stress, σ, can be calculated with Stoney's equation

$$\sigma = \frac{1}{6R}\frac{E}{1-\nu}\frac{t_s^2}{t_f}, \tag{3.5}$$

where E is the Young's modulus of the substrate, ν is Poisson's ratio, and t_s and t_f are the substrate and film thicknesses respectively [28]. Young's modulus for [100] silicon is $E = 180$ GPa [29], and the substrate thickness is provided by the manufacturer. The film thickness is calculated from the deposition rate and deposition time of the sputtering, which are calibrated prior to deposition.

Depending on the sign of σ, the stress is either compressive or tensile [28]. The two scenarios are shown in Figure 3.3.

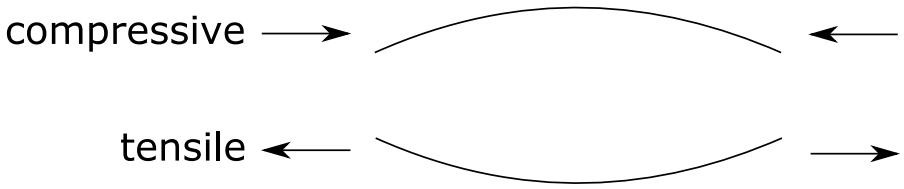

Figure 3.3: *Diagram showing how a substrate bends under compressive or tensile stress*

3.4 Wafer Cleaving

The thesis work requires that the wafers are cut in half for testing. To accomplish this, a scriber is used. The scriber consists of a moveable stage, microscope, and diamond-tipped scriber. The stage can move in the x- and y-directions, can rotate 90°, and also has a vacuum to hold the wafer in place. The microscope and moveable stage are used in conjunction to align the scribing with a crystal plane of the wafer. The flat edge of the wafer is used to align this. Once the wafer is aligned with a crystal plane, the stage is moved in the x-direction to place the diamond tip above the centre of the wafer. The diamond tip is then lowered to be in contact with the wafer, and the stage is moved in the y-direction. This creates a shallow scribe in the surface of the wafer along a crystal plane. The wafer is then removed from the stage, and pressure is applied to the back side of the wafer where the scribe was made. The pressure cleaves the wafer, and the scribe provides a path for the cleaving to occur. Since the scribing is aligned with a crystal plane, the cleaving follows a straight path.

3.5 Spectral Reflectance

The spectral reflectance measurement is a basic technique that gives the reflectance of your sample across a broad spectrum of wavelengths. The experimental setup is basic, and measurements are easy to perform. The setup can be seen in Figure 3.4.

A broad spectrum light source is used with light in the visible and near-infrared range. The light is coupled to the outer cores of a multi-core, multi-mode fiber. The light then passes from the fiber, through a collimator, and onto the surface of the sample mirror with normal incidence. The reflected light then travels back through the collimator and into the fiber. The central core of the fiber then goes to an Optical Spectrum Analyzer (OSA) [23]. The OSA measures the amount of reflected light from the central core at each wavelength to get the reflectance across a broad spectrum of light. Since the light source does not have uniform intensity across all wavelengths, a reference sample with known reflectivity is required to normalize the reflectivity of the sample mirror. The reference mirror used is 100 nm of gold evaporated on a wafer. It has a reflectivity of approximately 98 % across the wavelengths used. In addition, the background light can be filtered out by performing the same measurements with the light source off. In total, 4 measurements are performed to get the final result. These are measurements with the

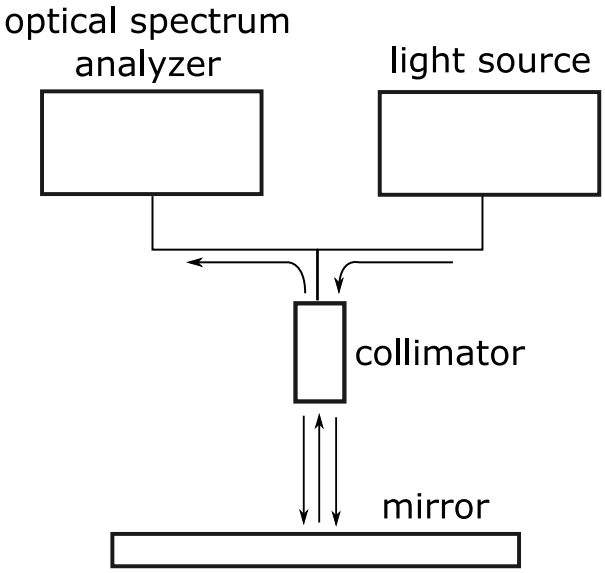

Figure 3.4: *Spectral reflectance setup to measure reflectance of sample across many wavelengths.*

light source on and off for both the reference and sample mirrors. The spectral reflectance, $R(\lambda)$, can then be calculated by

$$R(\lambda) = \frac{I_{sl}(\lambda) - I_{sd}(\lambda)}{I_{rl}(\lambda) - I_{rd}(\lambda)} R_r, \tag{3.6}$$

where I_{sl}, I_{sd}, I_{rl}, and I_{rd} are the spectral light intensity distribution of the reflected light for the sample mirror with the light source on, the sample mirror with the light source off, the reference mirror with the light source on, and the reference mirror with the light source off respectively. R_r is the known reflectivity of the reference mirror across the spectrum.

This method has a few drawbacks that limit its effectiveness in determining the reflectance. For one, it requires a reference mirror with a well-known reflectance across the whole spectrum of light being used. In addition, the OSA must switch between photodetectors at 1000 nm since the gain of silicon photodetectors drops off past this point. This is very close to the wavelength of interest of 980 nm. The results often show a step in level when the detector changes, so it is hard to tell what the real reflectance is in this region. In addition, only one reading with light incident on the mirror is used to determine the reflectance, leaving this method susceptible to noise and error.

3.6 Absolute Reflectance

Knowing the precise value of the reflectance of a DBR is very important since the reflectance must be $> 99\%$ for VCSELs. Also, it will determine how much power you get out of your overall device. If the reflectance of the mirror is not known well, then when testing fabricated VCSELs it would be unclear if seeing poor performance was because the mirror is not as good

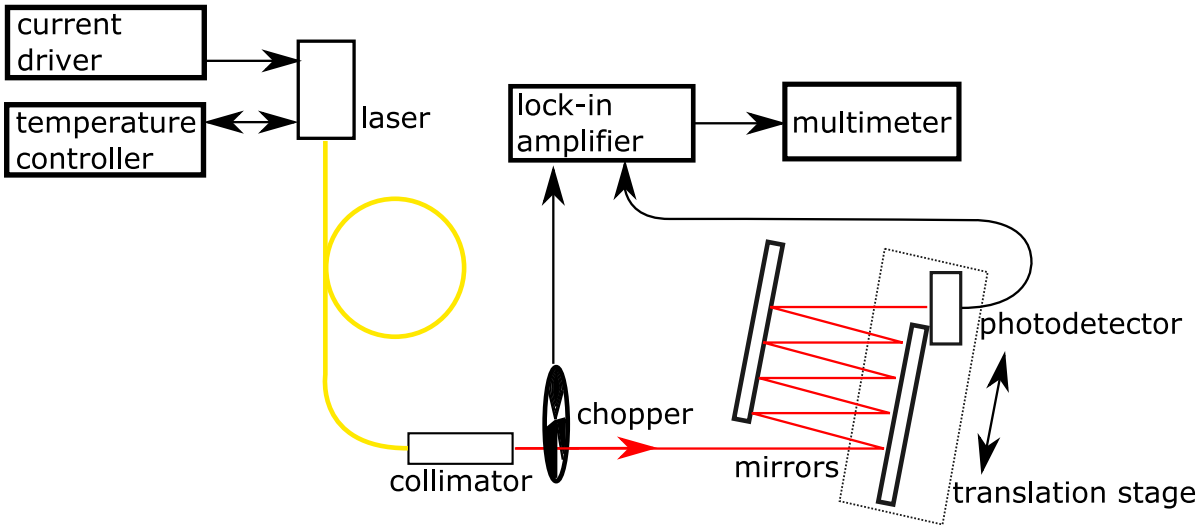

Figure 3.5: *Experimental setup for z-method to measure absolute reflectance.*

as intended, or if it is due to some other effect in the device. Knowing the reflectance very well helps in designing and analyzing the measured results from VCSELs. As a result, there is a need for a method more precise than the spectral reflectance method presented in Section 3.5.

For this thesis, a new setup was built to characterize the absolute reflectance of the deposited DBRs at the wavelength of interest. The method used is called the z-method and is described in [30]. It uses multiple bounces of the laser beam on two mirrors. The bounces make a 'z' shape, hence the name z-method. A schematic of the setup can be seen in Figure 3.5.

For the z-method, a laser at a given wavelength is coupled to a fiber. The light is then collimated, and the beam bounces back and forth on the mirrors, before hitting a photodetector measuring the beam power. One of the mirrors is placed on a translating stage that will keep it parallel with the other mirror. By translating the mirror, you can select the number of bounces the beam will take (always a multiple of 2) before reaching the photodetector. By taking a reading of the power at each multiple of two bounces, as well as the power for zero bounces, the reflectance of the mirrors can be extracted.

The power after N bounces is given by

$$P_N = P_0(R_1R_2)^{N/2}, \tag{3.7}$$

where P_0 is the output power of the laser, and R_1 and R_2 are the reflectances of the respective mirrors. Each mirror individually sees $N/2$ bounces. By cleaving the deposited mirrors in two, the need for a reference mirror is removed, and the equation becomes

$$P_N = R^N P_0. \tag{3.8}$$

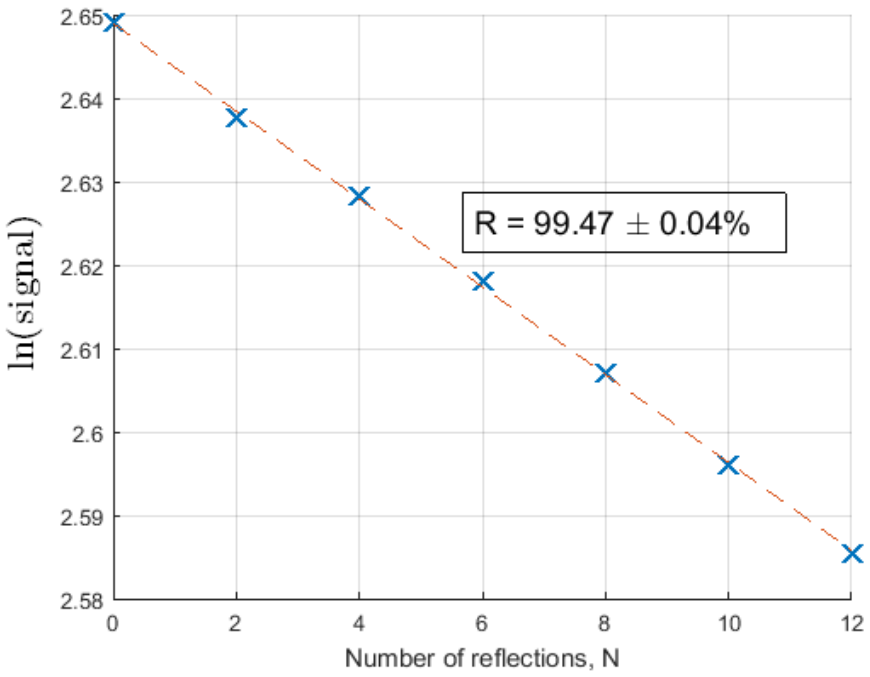

Figure 3.6: *Graph of ln(signal) vs. N for data measured using z-method as an example of how the reflectance is extracted from the measured data points.*

To get the reflectance, R, Equation 3.8 is linearized to become

$$\ln P_N = N \ln R + \ln P_0. \tag{3.9}$$

By fitting a line of best fit to Equation 3.9, the value of R can easily be extracted from the slope of the fit, $\ln R$. An example of the data extraction is seen in Figure 3.6 showing a plot of the linearized data along with the line of best fit.

The error on the results is taken from the method in [30]. The relative error in the reflectance $(\frac{\Delta R}{R})$ is given by

$$\frac{\Delta R}{R} = \frac{2\Delta X}{N_{max}} + r, \tag{3.10}$$

where ΔX is the relative detection noise measured through the system, N_{max} is the maximum number of bounces, and r is the reproducibility factor. The reproducibility factor is a measure of how well the results are reproduced for different measurements of the same mirror. A number of steps were taken to lower the error in the design of the setup. To reduce ΔX, a lock-in amplifier was used to filter out any background light and to remove any drift caused by the detector. In addition, the detector was mounted on the same translating stage as the mirror. This means the beam will always hit the detector at the same spot to reduce any effects of the

detector having different sensitivity over its surface. Also, it is seen that the error is inversely proportional to N_{max}, so the system was designed to achieve as many bounces as possible. This was done by collimating the light to a small beam size (2 mm), and spacing reflections closely together (3 mm). The beam spacing had to be larger than the beam size since the cleaving process causes defects in the mirror at the cleaved edge, so a small margin of error was kept to keep the beams away from this area. This easily allows 12 total reflections to occur, which covers a distance of 18 mm on each mirror.

A large area silicon photodetector is used mainly since Si photodiodes have peak photosensitivity around the 980 nm region that is targeted here [31]. In addition, a larger area means additional optics like a focusing lens are not needed to focus the beam on the detector. The photodiode used is model S2281 from Hamamatsu.

To reduce noise in the results, a slow integration time is used in addition to averaging 15 consecutive readings before displaying the result on the multimeter.

The laser is driven by a current source providing a constant drive current. To maintain the same optical power, a temperature controller is used to maintain the laser at a constant temperature. The constant temperature and constant current lead to a constant output power.

While this method is much improved over the spectral reflectance method presented, it is not perfect. Since multiple bounces are used over the surface of the mirror, the overall reflectance measured is an average of the reflectances from each bounce instead of the reflectance at a specific point. In addition, to get the multiple bounces, the laser must be incident at an angle instead of normal incidence. The effect of this is kept minimal by using a small angle (1.5°), and when the light enters the mirror from air, it will be refracted to an even smaller angle.

3.6.1 Lock-in Amplifier

A lock-in amplifier can be used in the design to reduce error in the measurements. The lock-in amplifier works in conjunction with an optical chopper, and enables detection only at a specific frequency. The optical chopper takes a continuous wave input, and "chops" the light into a square wave with a 50% duty cycle. This is done with a rotating wheel at a fixed frequency that will either block or transmit the beam through half of the time. Light from the desired source will then be incident on the detector with a known frequency. The lock-in amplifer can then filter out any signal at a different frequency to leave only the laser beam's signal. This means that any background light affecting the results is filtered out, as well as any drift that may be present in the detector since these sources of error have a very small chance of having the same frequency as the desired signal [32].

The lock-in amplifier functions by multiplying the input signal by a reference signal at the same frequency as the optical chopper. The input signal contains the data we want to extract at the reference frequency, as well as any noise that will largely be at other frequencies. By multiplyng the signals together, and integrating over a large enough time scale, any signal not at the reference signal will be attenuated to zero. To get a non-zero output for the desired signal, the reference signal must be in phase with the desired signal, so a phase shift is introduced to

the reference signal. What is left is a DC signal proportional to the magnitude of the signal we want to detect. V_{out}, the output voltage of the lock-in amplifier is then given by

$$\begin{aligned} V_{out} &= A\cos(\omega t)B\cos(\omega t + \theta) \\ &= \frac{1}{2}AB\cos(\theta) + \frac{1}{2}AB\cos(2\omega t + \theta) \end{aligned} \tag{3.11}$$

where A and B are the amplitudes of the input signal (at the reference frequency) and reference signal respectively, ω is the angular frequency of the reference signal, and θ is the phase introduced by the lock-in amplifier to match the phase of the input and reference signals. V_{out} consists of a DC signal and a signal oscillating at twice the reference frequency. The oscillating signal is removed by a low-pass filter at the output of the lock-in amplifier to leave only a DC signal. B is kept constant, and the result is an output voltage proportional to A. Equation 3.11 shows how a sinusoidal signal is detected, however for the case of using an optical chopper, a square wave signal is produced. The output voltage for this case is done in much the same way, however the signal is also multiplied by odd harmonics of ω to capture the whole square wave in the output. This is done through a setting on the lock-in amplifier [32].

Chapter 4

Materials for DBRs

This chapter will discuss the requirements for choosing DBR materials for VCSELs, a comparison of using semiconductor vs. dielectric materials, and a discussion of the low and high index of refraction materials chosen for this work.

4.1 Material Requirements

Since VCSELs require DBRs with $R > 99\,\%$, a number of strict demands are placed on the materials used. To achieve high reflectances, the contrast in refractive index must be high, there must be low optical loss, and interfaces must be abrupt.

In addition, VCSELs place some other considerations on DBR materials like penetration depth of the optical field into the DBR [4], and the materials chosen should be able to be easily incorporated into existing semiconductor process flows.

A higher contrast in refractive index means more reflection occurs at each interface as described in Equation 2.4, and as a result higher reflectances are able to be achieved with less DBR pairs. A higher contrast in n also lowers the penetration depth of the optical field into the mirror, meaning there is increased optical confinement of light in the active (gain) region of the VCSEL [4]. This allows more photons to be available to stimulate more photon emission. Futhermore, the stopband width is increased with larger contrast in n, allowing easier spectral matching of gain and cavity resonance.

In addition to a high contrast in n, the materials should have very low optical loss around the operating wavelength of the DBR. Since such high reflectances are required for lasing of VCSELs, this is a very strict requirement in choosing materials. Any significant absorption in the mirror will lower its reflectance and/or cause too little light to be transmitted out of the laser.

Interfaces should be abrupt, and with little surface roughness. The Fresnel equations presented in Section 2.2.1 assume abrupt interfaces. In addition, appreciable surface roughness of dielectric layers has been shown to increase absorption in dielectric DBRs [24].

4.2 Semiconductor vs. Dielectric

This section will compare semiconductor and dielectric DBRs for each of the requirements needed for VCSEL DBRs outlined above.

Semiconductor DBRs are currently the DBR of choice for VCSEL fabrication, however dielectric DBRs are being explored to replace one or both of the semiconductor DBRs in VCSELs since they provide a number of advantages.

Note that when referring to 'semiconductor DBRs' here, what is meant is 'epitaxially grown semiconductor DBRs'. In addition, a loose definition of dielectric materials is used to refer to materials that are largely insulators, and can be deposited with sputtering.

4.2.1 Refractive Index Contrast

The materials for semiconductor DBRs are limited due to lattice matching requirements, and as a result it is difficult to achieve high contrast in DBR layers. For example, a stack of GaAs/AlAs has a contrast of

$$\frac{\Delta n}{n} = \frac{n_{GaAs} - n_{AlAs}}{n_{GaAs}} = \frac{3.5160 - 2.9514}{3.5160} = 16\,\%$$

at 980 nm [33] [34]. As a result, 20 or more pairs can be required to achieve $> 99\,\%$ reflectance [17]. This small contrast leads to a larger penetration depth into the mirror, and a narrower stopband as well.

Dielectric materials are not crytalline, so lattice matching is not a constraint on material choice. As a result, materials are able to be more freely chosen to get large contrast in layers. For example, a stack of SiO_2/TiO_2 has a contrast of

$$\frac{\Delta n}{n} = \frac{n_{TiO_2} - n_{SiO_2}}{n_{SiO_2}} = \frac{2.4880 - 1.4676}{1.4676} = 70\,\%$$

at 980 nm [35] [36]. This large contrast allows fewer pairs, smaller penetration depth, and a wider stopband which are all beneficial to VCSEL operation.

4.2.2 Optical Loss

The minimum optical loss of semiconductor DBRs is fundamentally limited by free-carrier absorption since they are conductive [4]. Free-carrier absorption is where an already excited charge carrier is further excited by absorbing a photon. This leads to photons lost that cannot be used for lasing. In addition, in typical VCSEL processes, semiconductor DBRs are p-doped for the top reflector and n-doped for the bottom reflector to provide carrier injection to the active region. The dopants cause defects in the crystalline layers where photons can be scattered and lost [37].

Dielectric materials on the other hand are electrical insulators, and do not suffer from free-carrier absorption. As a result, they can have an extinction coefficient of zero. Additionally, there are no dopants present to cause scattering. This is a huge benefit for VCSEL DBRs to achieve high reflectances with no absorption.

4.2.3 Interfaces

Semiconductor DBRs are grown epitaxially with lattice matched layers. Proper lattice matching ensures the interfaces are distinct and free of defects like dangling bonds. Dielectric DBRs on the other hand are deposited using sputtering, and are able to achieve distinct layers as well so long as the sputtering deposition parameters have been optimized for the chosen material. Both types are able to achieve the abrupt interfaces required for VCSEL DBRs.

4.2.4 Conclusion

Dielectric DBRs offer some distinct advantages over semiconductor DBRs for VCSELs due to their much higher n contrast and lower absorption. Both can be made with abrupt interfaces between layers.

4.3 Low Refractive Index

SiO_2 is the natural choice for low index of refraction material. It offers the lowest n of the dielectrics able to be sputtered at Chalmers with reported values of $n = 1.4676$ and $\kappa = 0$ at 980 nm [35]. In addition, it is extensively used in semiconductor fabrication, and is therefore well known and well understood. Silicon is not very electrically conducting in its pure form and since we are depositing SiO_2, oxygen is needed as a reactive gas. Therefore reactive RF magnetron sputtering is used.

Figure 4.1 shows a typical plot of n and κ measured with ellipsometry for a sputtered thin-film of SiO_2.

4.4 High Refractive Index

Since SiO_2 was chosen as the low refractive index material, any materials based on nitrides are ruled out for use as high refractive index material due to the limitation of the sputtering tool used since it is time-consuming to switch between oxygen and nitrogen for reactive sputtering as explained in Section 3.1. In addition, the targets available for the sputtering tool limit the materials that can be deposited. Available dielectrics to be sputtered with these constraints are amorphous silicon (a-Si), TiO_2, Ta_2O_5, and HfO_2. A summary of reported n and κ for each of these materials can be found in Table 4.1.

Table 4.1: *n and κ values at 980 nm for various high refractive index materials available for sputtering using FHR MS150 tool.*

Material	n(980 nm)	k(980 nm)	References
a-Si	3.6568	0	[38]
TiO_2	2.4880	0.00010 (1.54 μm)	[36] [39]
HfO_2	2.0840	-	[40]
Ta_2O_5	2.0809	0.0016161	[41]

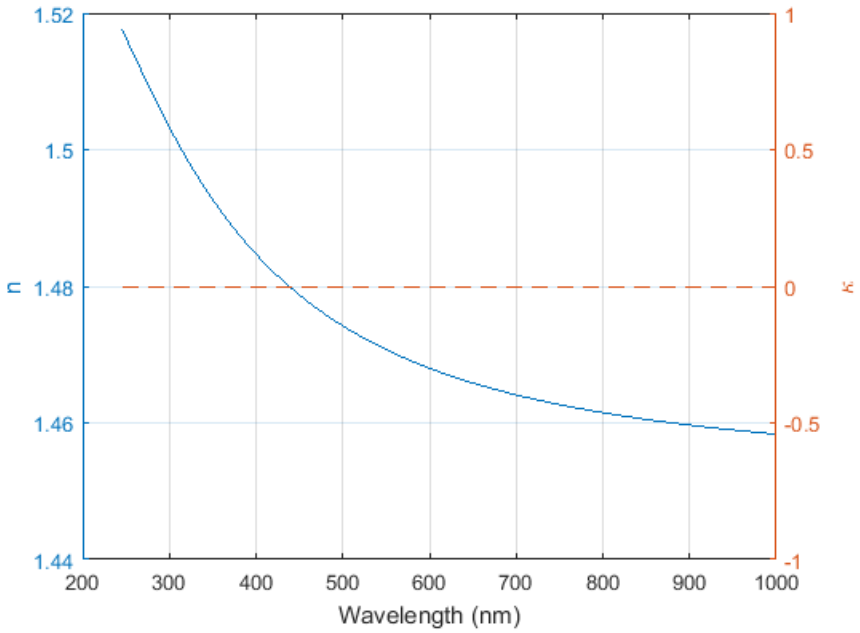

Figure 4.1: *n and κ vs. wavelength for ellipsometry measurement of sputtered SiO_2 thin-film.*

The two materials with the highest n at 980 nm are a-Si and TiO_2. In addition, it is reported these materials have an extinction coefficient of 0 (or close to 0) at 980 nm. That makes these ideal to use as the high index of refraction material, and both will be used in this work. Figure 4.2 shows a typical plot of n and κ measured with ellipsometry for sputtered thin-films of TiO_2 and a-Si.

TiO_2 has been successfully incorporated into fabrication processes to make memristors [42]. In addition, it has been used successfully in dielectric DBRs for VCSELs at Chalmers [43] and elsewhere [44]. Since titanium is a metal, and an oxide is being deposited, reactive DC magnetron sputtering is used with O_2 as the reactive gas.

a-Si is a very common material used in photovoltaics [45], and is also used as the active layer in thin-film transistors [46]. It has also been used in DBRs [47]. As in the case for depositing SiO_2, RF sputtering is needed. There is no reactive gas required for depositing a-Si, so RF magnetron sputtering is used. It is reported that the optical properties of sputtered a-Si are very dependent on the deposition parameters used while sputtering [48].

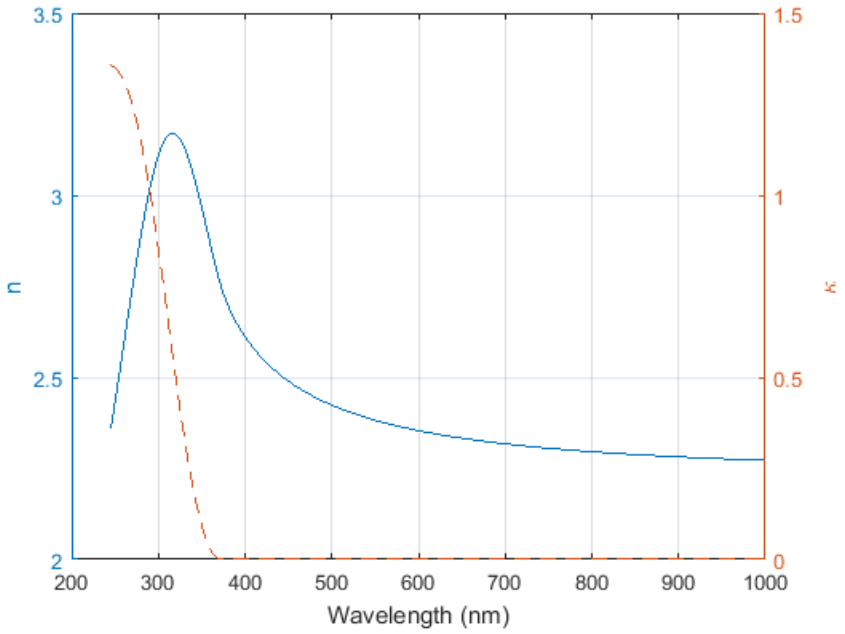

(a) TiO_2

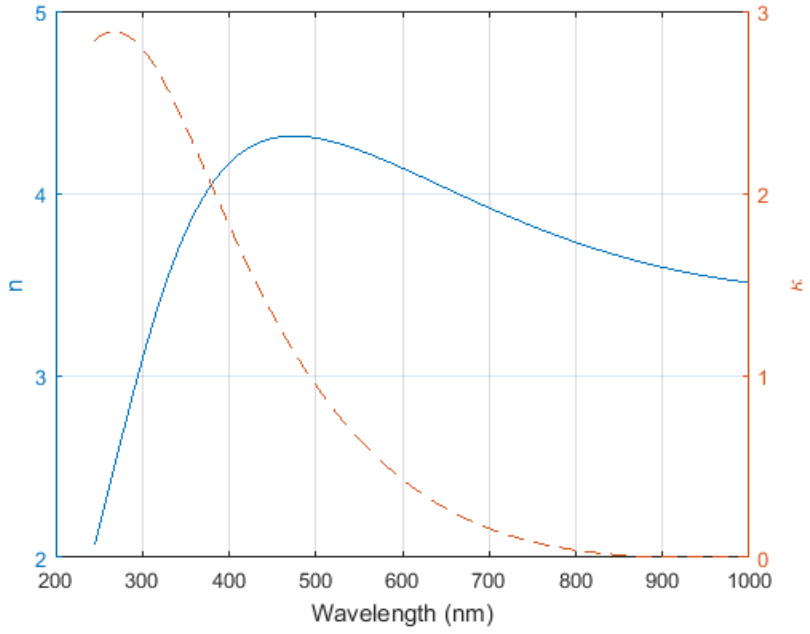

(b) *a-Si*

Figure 4.2: *n and κ vs. wavelength for ellipsometry measurement of sputtered thin-films of (a) TiO_2, and (b) a-Si.*

Chapter 5

Results and Discussion

This chapter presents the results obtained and discusses their meaning and impact.

5.1 Error Estimate for z-Method

As in Section 3.6, Equation 3.10, the relative error in the reflectance ($\frac{\Delta R}{R}$) is determined by the relative detection noise (ΔX), the maximum number of reflections (N_{max}), and the reproducibility factor (r)

$$\frac{\Delta R}{R} = \frac{2\Delta X}{N_{max}} + r.$$

N_{max} should be made as large as possible to reduce the error. The constraints for the system are the size of the mirrors (25.4 mm) and the beam spacing (3 mm). This allows up to 8 reflections on each mirror, however for practical purposes only 6 reflections on each mirror are used since more reflections imposes even stricter alignment of the stages, and the reflectance of the mirrors at the wafer edges is not as reliable. 12 total bounces was the tradeoff chosen to achieve small error with an easy-to-use setup.

The relative detection noise is a measure of the noise throughout the system, and the reproducibility factor represents with what accuracy a result is able to be reproduced by the setup.

5.1.1 Relative Detection Noise

To determine the relative detection noise of the system, we want to look at how much the detected signal can change over the timeframe of one measurement. To do the measurement, the entire system was used with the optical chopper, 12 total bounces on the mirrors, the photodetector, the lock-in amplifier, and the multimeter. The settings on the lock-in amplifer, laser, multimeter, and optical chopper were set to how they would be used in the real measurements. This way the setup mirrored the real measurements. The test was done for 15 hours, with a computer taking a reading of the detected signal from the multimeter every 10 seconds. The recorded signal is seen in Figure 5.1.

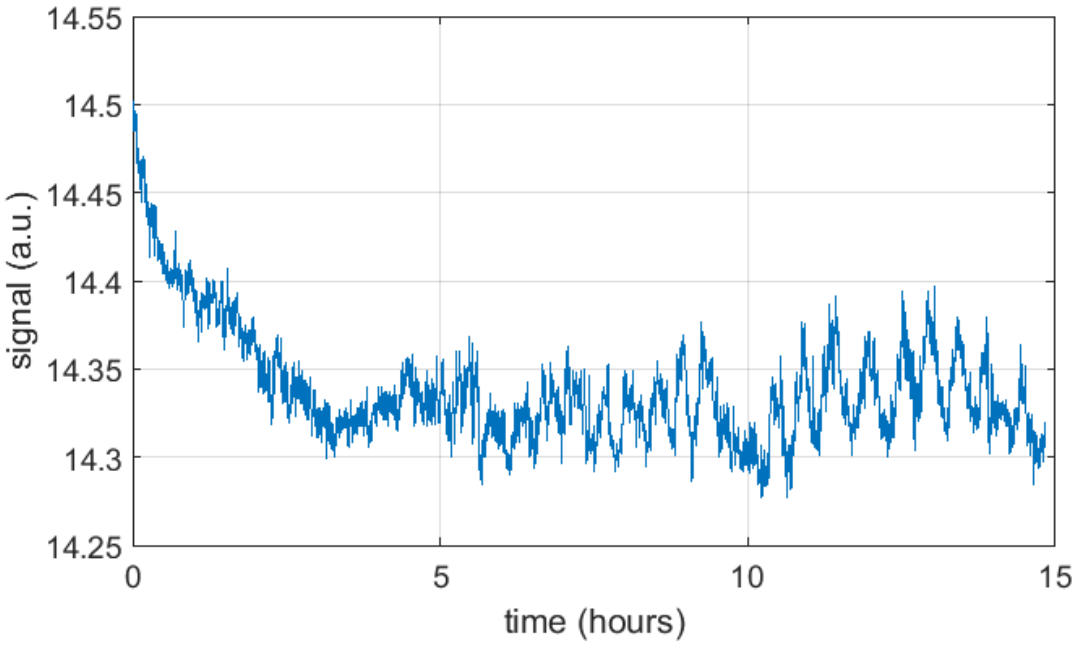

Figure 5.1: *Signal vs. time for measured signal through system for evaluation of system noise.*

A complete measurement of one mirror sample takes less than 5 minutes (typically around 3 minutes) from recording the initial measurement for no reflections to the maximum of 12 reflections. This is after the initial time spent to align the setup with the sample mirror. To determine the relative detection noise, the measurement was then divided into 10 minute segments. 10 minutes was chosen since it is a bit longer than the measurement time, and will thus provide a slight overestimation of the error in the system since there is more time for the signal to deviate from its starting point. Within each 10 minute segment, the relative error for that block was calculated as the standard deviation over the mean, $\Delta X = {}^{\sigma}/_{\mu}$. To get a more reliable estimation of the detection noise, the relative error for each 10 minute block was then averaged to get ΔX_{avg}, the relative detection noise of the system. This was found to be $\Delta X_{avg} = 0.000725 \pm 0.000274$. If we again take the worst case, and use the mean plus the standard deviation, we get $\Delta X_{avg} = 0.000999 \simeq 0.0010$.

5.1.2 Reproducibility

To evaluate how reproducible a single result is using the z-methed measurement setup constructed, the measurements were repeated 10 times on a single mirror. The mirror used was a 6-pair SiO_2/TiO_2 DBR that was fabricated during this work. To ensure each of the 10 measurements were independent of each other, the setup was intentionally misaligned and then realigned at the start of each set of measurements. This removes any systematic error that could be present from measuring repeatedly at a specific alignment of the stages in the setup. The alignment

Table 5.1: *Measurement of R for 10 trials of the same mirror using z-method for evaluation of reproducibility of system. R_{avg} is reported along with its standard deviation.*

Trial	R (%)
1	99.45
2	99.41
3	99.41
4	99.42
5	99.40
6	99.45
7	99.42
8	99.41
9	99.44
10	99.47
R_{avg}	99.43 ± 0.02

consists of the angle of the laser, the angles of the two mirrors, and the positions of the mirrors. The mirrors were also removed and remounted between trials. The results of the ten trials can be seen in Table 5.1.

The average reflectance and standard deviation of the 10 trials is $R_{avg} = 99.43 \pm 0.02\,\%$. The reproducibility factor is then taken as the relative error on this measurement and is $\sigma_{R_{avg}}/R_{avg} = 0.0002$.

5.1.3 Lock-in amplifier vs. no lock-in amplifier

The lock-in amplifer serves to lower the noise in the system by filtering out the detector drift and background light, leaving only the laser beam signal. One drawback however is that the optical chopper essentially cuts the beam in half, so only half of the power reaches the detector. Lower power at the detector means that any noise in the system will have a larger impact on the results.

The same method to calculate the relative detection noise used for the lock-in amplifier was also done without the lock-in amplifier. This yielded a final result of $\Delta X_{avg} = 0.0014$. This is very close to that found for using the lock-in amplifier which was $\Delta X_{avg} = 0.0010$, meaning that using the system without the lock-in amplifier is also viable to achieve good results. However, to use the system without the lock-in amplifer increases the complexity of measurement taking. Either the measurement should be performed in a dark room, making the measurements more difficult and limiting use of the room while the measurement is taking place, or a background noise reading should be taken, and then subtracted from the results. This is still susceptible to detector drift, and a background reading should be taken close in time to each data point measured to account for drift during the whole measurement.

5.1.4 Conclusion

The final error on the z-method results using the lock-in amplifer is then

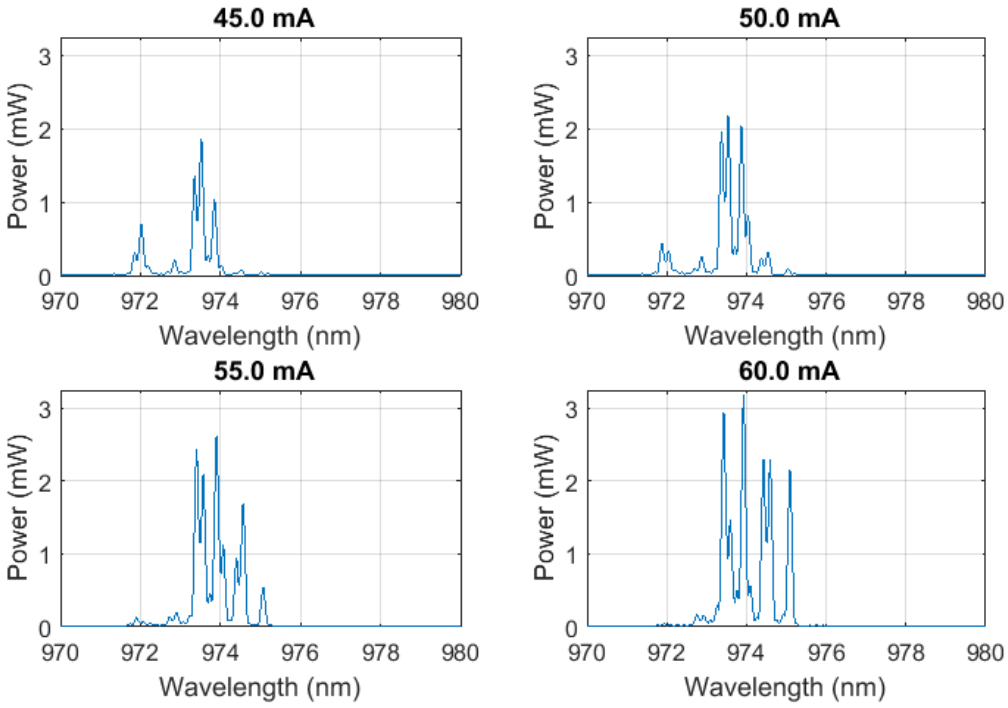

Figure 5.2: *Power vs. wavelength for laser driven at 45, 50, 55, and 60 mA at 25° C.*

$$\frac{\Delta R}{R} = \frac{2\Delta X}{N_{max}} + r = \frac{2 \cdot 0.0010}{12} + 0.0002 = 0.0003667 \simeq 0.0004 = 0.04\,\%,$$

and without using the lock-in amplifier is

$$\frac{\Delta R}{R} = \frac{2\Delta X}{N_{max}} + r = \frac{2 \cdot 0.0014}{12} + 0.0002 = 0.0004333 \simeq 0.0004 = 0.04\,\%.$$

In the end, it is preferred to use the lock-in amplifier since the measurements are simpler to take and the error is a slightly better. All measurements reported in this thesis make use of the lock-in amplifier.

5.1.5 Laser Output Power

An important choice is what current to drive the laser with since this will set the output power of the laser. The laser used is a fiber-coupled Fabry-Perot laser with emission around 980 nm. The laser is temperature controlled to remain at 25°C. A number of different drive currents were tested to see the modal response of the laser. The results of these tests can be seen in Figure 5.2.

If the peak wavelength is not directly at 980 nm it can still be used since the stop band for DBRs, and specifically dielectric DBRs, is quite wide so the reflectance at wavelengths near the

target of 980 nm will be indistinguishable. 60 mA was chosen to be the drive current since it lases a bit closer to 980 nm than the other drive current. In addition, it provides more power than the others meaning a larger percentage of the detected signal will be due to the laser beam as opposed to noise in the system. This means the relative error on the detected signal goes down. Too high power should be avoided since it poses safety risks, and can damage some of the equipment used if it exceeds the specifications.

5.2 Deposition Results

This section shows the deposition parameters used to deposit each of the materials used. In addition, it shows an example of data from the ellipsometer collected from one of the deposited samples, and summarizes the optical properties of the calibration runs performed. The calibration run is performed to determine the n, κ, and deposition rate parameters prior to depositing a DBR. These runs need to be performed since film properties can change over time as the target material wears down in the machine. The three parameters are determined using ellipsometry. The deposition rate is calculated by measuring the layer thickness, d, and dividing by the deposition time. The n value measured is then used to determine the target layer thickness to achieve the $^{\lambda}/_{4}$ condition. Once the desired thickness is calculated, the deposition time can be calculated using the measured deposition rate.

5.2.1 SiO_2

The parameters for the standard recipe used at Chalmers to deposit SiO_2 using the FHR MS150 tool are summarized in Table 5.2. The unit 'sccm' is standard cubic centimeter per minute and is used for mass flow of the sputtering and reactive gasses.

Table 5.2: *Standard sputter deposition parameters for SiO_2.*

Parameter	Value
RF power	1.0 kW
Ar flow	40.0 sccm
O_2 flow	15.0 sccm
Pressure	$1.3 \cdot 10^{-2}$ mbar

In total, 10 calibration runs for SiO_2 were performed over the course of this thesis, and their results are summarized in Table 5.3 for 980 nm. Note that κ was zero for each case.

The time to deposit one layer of SiO_2 with these results is $\approx$ 740 s. The thickness of one layer is then $\approx$ 169 nm.

The average stress in a single layer of SiO_2 on silicon with thickness corresponding to $^{\lambda}/_{4}$ was measured to be -13.70 MPa, corresponding to a compressively stressed film.

Table 5.3: *Ellipsometer data for n(980 nm) and deposition rate for sputtered SiO_2 films. Average, standard deviation, and relative error are also presented.*

Trial	n(980 nm)	deposition rate (nm/s)
1	1.4497	0.2298
2	1.4484	0.2273
3	1.4480	0.2248
4	1.4459	0.2293
5	1.4445	0.2311
6	1.4469	0.2342
7	1.4454	0.2327
8	1.4452	0.2337
9	1.4586	0.2202
10	1.4555	0.2195
average	1.4488 ± 0.0047	0.2283 ± 0.0053
relative error	0.3%	2.3%

5.2.2 TiO_2

The parameters for the standard recipe used at Chalmers to deposit TiO_2 using the FHR MS150 tool are summarized in Table 5.4. In total, 5 calibration runs for TiO_2 were performed, and their results are summarized in Table 5.5 for 980 nm. Note that κ was zero for each case. The time to deposit one layer is ≈ 840 s, and the layer thickness is ≈ 107 nm.

Table 5.4: *Standard sputter deposition parameters for TiO_2.*

Parameter	Value
DC power	1.0 kW
Ar flow	40.0 sccm
O_2 flow	5.0 sccm
Pressure	$5.0 \cdot 10^{-3}$ mbar

Table 5.5: *Ellipsometer data for n(980 nm) and deposition rate for sputtered TiO_2 films. Average, standard deviation, and relative error are also presented.*

Trial	n(980 nm)	deposition rate (nm/s)
1	2.3022	0.1300
2	2.2907	0.1260
3	2.2577	0.1285
4	2.2677	0.1261
5	2.2738	0.1286
average	2.2784 ± 0.0179	0.1278 ± 0.0017
relative error	0.8%	1.3%

The average stress in a single layer of TiO_2 deposited on silicon was measured to be 214.2 MPa, corresponding to tensile stress. The average stress for a 1-pair DBR of SiO_2/TiO_2 was measured to be 80.63 MPa, while the average stress measured in a 6-pair SiO_2/TiO_2 DBR was 49.12 MPa. This lowering of the stress suggests there is a compensating effect of depositing alternating layers of compressively stressed (SiO_2) and tensilely stressed (TiO_2) materials. This results in an overall lowering of the stress in the stack.

5.2.3 a-Si

The parameters for the standard recipe used at Chalmers to deposit a-Si using the FHR MS150 tool are summarized in Table 5.6. Note that these are identical to those used for SiO_2 except that there is no reactive gas used here. Little work with a-Si has been done with this machine at Chalmers, so the parameters are not as refined as those used for SiO_2 and TiO_2.

Table 5.6: *Standard sputter deposition parameters for a-Si.*

Parameter	Value
RF power	1.0 kW
Ar flow	40.0 sccm
Pressure	$1.3 \cdot 10^{-2}$ mbar

These initial parameter yielded some interesting results. Since a-Si has a very high refractive index, it requires thin layers (≈ 70 nm). It was found that the deposition rate is around 0.65 nm/s, which leads to very short deposition times of around 105 s. This is both intriguing and worrying at the same time. Since it is so quick, it drastically speeds up the deposition time for DBRs, and is roughly 8 times faster than depositing TiO_2. At the same time, however, it could be too quick causing less reliability in the layer thickness which could negatively impact the overall reflectance of the mirrors. This prompted some further investigation, where the deposition rate was attempted to be slowed down by changing deposition parameters.

Three RF powers were tried, 0.33 kW, 0.5 kW, and 1.0 kW. These gave deposition rates of 0.095 nm/s, 0.205 nm/s, and 0.65 nm/s respectively. In the end, it was decided to make the mirrors with 0.5 kW RF power since it was a good trade off between speed and reliability, and this rate is more in line with those of SiO_2 and TiO_2. In addition, a 6-pair DBR using 1.0 kW was also produced for comparison's sake.

In total, 3 calibration runs for a-Si were performed for 0.5 kW, and their results are summarized in Table 5.7 for 980 nm along with the results of the test runs for 0.33 kW and 1.0 kW. Note that κ was not measured with the ellipsometer for each case. The ellipsometer can provide values for n and d accurately, however for a-Si it is difficult to get a reliable reading of κ. As such, an estimate of the value for κ can still be determined from simulations using the measured n values from the ellipsometer and sweeping κ until the simulated $R(980\,\text{nm})$ value matches best with the z-method measurement for $R(980\,\text{nm})$. This provides an estimate for κ, however other loss factors are lumped into this as well (see Section 5.4 for more detail).

Table 5.7: *Ellipsometer data for n(980 nm) and deposition rate for sputtered a-Si films. Results are presented for RF powers of 1.00, 0.50, and 0.33 kW. Average, standard deviation, and relative error are presented for the 0.50 kW results.*

Trial	n(980 nm)	deposition rate (nm/s)
(1.00 kW) 1	3.6346	0.6585
(0.33 kW) 1	3.1162	0.0967
(0.50 kW) 1	3.4222	0.2067
2	3.5594	0.2207
3	3.7300	0.2143
(0.50 kW) average	3.5705 ± 0.1542	0.2139 ± 0.0070
relative error	4.3%	3.3%

The average stress measured in a pair of SiO_2/a-Si layers was -61.01 MPa, and for a 6-pair stack was -209.2 MPa. This suggests that the compressive stresses in both the SiO_2 and a-Si layers build up the overall stress in the stack as layers are added.

5.2.4 Fabrication Reliability

After seeing how the optical properties can change for each material between depositions using the same sputtering parameters, a question was posed about how these changes could effect the overall reflectivity of the DBR, since each layer could have slightly different n, κ, and d values. As a result, simulations were performed allowing each layer to vary these parameters. The average results found from the depositions that are reported in Sections 5.2.1, 5.2.2, and 5.2.3 were used as a starting point for the variations. Each layer began with the average values, and was then individually varied based on the standard deviation of the average. The variation was allowed to be larger than the standard deviation to reflect a worst case scenario. The variation is randomly chosen from $-$*allowed variation* to $+$*allowed variation*.

The simulations were performed for 2-8-pair mirrors, and 10 000 iterations were done for each. For both sets of materials, two simulations are performed, one a poor case with variations a little bit larger than observed, and a worst case with variations allowed up to twice those of the poor case. The simulations are done only for reflectance at 980 nm.

The variations allowed for each material for both cases are shown in Table 5.8 for n and Table 5.9 for d. An example of a distribution obtained is shown in Figure 5.3 for a 6-pair SiO_2/TiO_2 DBR.

Table 5.8: *Relative error for n(980 nm) from deposition results and allowed ± variations for poor case and worst case of each layer for fabrication reliability simulations.*

Material	actual (%)	poor case (%)	worst case (%)
SiO_2	0.3	1.0	2.0
TiO_2	0.8	2.0	4.0
a-Si	4.3	5.0	10.0

Table 5.9: *Relative error for d from deposition results and allowed ± variations for poor case and worst case of each layer for fabrication reliability simulations.*

Material	actual (%)	poor case (%)	worst case (%)
SiO_2	2.3	5.0	10.0
TiO_2	1.3	3.0	6.0
a-Si	3.3	5.0	10.0

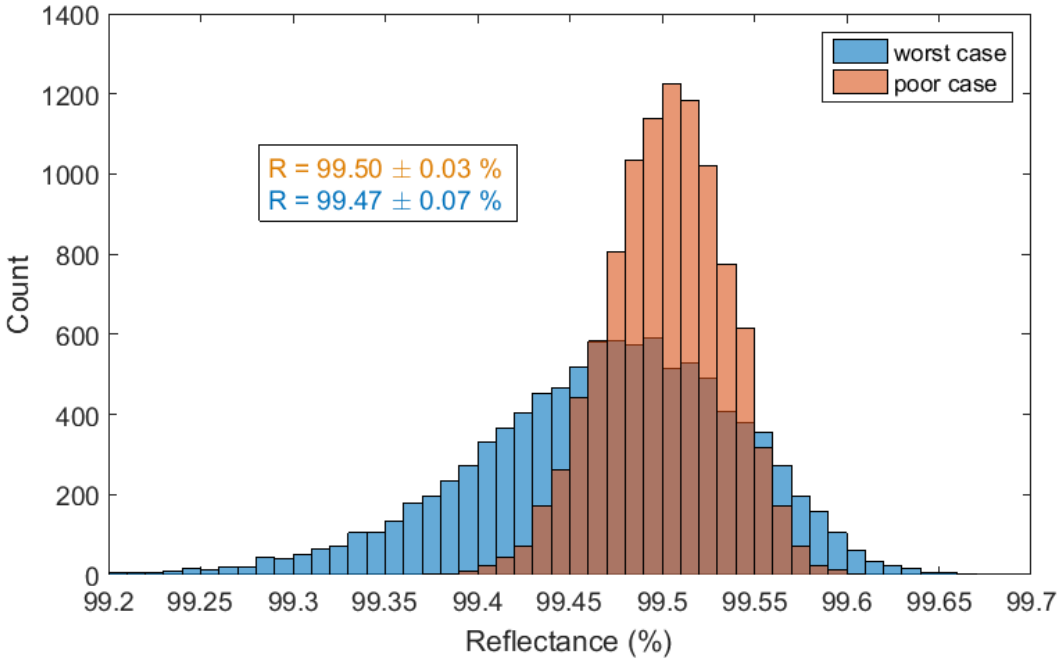

Figure 5.3: *Histograms of poor and worst case simulations for 6-pair SiO_2/TiO_2 mirrors.*

For 6-pair SiO_2/TiO_2 DBRs, it is seen that the deposition parameters used are reliable, and do not alter the resulting reflectance too much. The poor case results in $R = 99.50 \pm 0.03\%$, whereas a simulation for the same values, but with no variation yields $R = 99.51\%$. All simulations achieved over 99 % reflectance which means the deposition parameters used are very reliable for VCSEL DBRs.

An example of the results of the reliability simulations for SiO_2/a-Si DBRs is shown for 6 pairs in Figure 5.4. The data for a deposition with an RF power of 0.50 kW is used for these simulations, and note that a constant value for $\kappa = 0.015$ is used. This value comes from the measured results that will be presented in Section 5.4. The extinction coefficient was kept constant as opposed to varied since there is too little data to properly assess how much variation is reasonable.

For 6-pair SiO_2/a-Si DBRs, it is seen that the deposition parameters used are less reliable as there is a larger spread in reflectances, and some mirrors have less than 99 % reflectance.

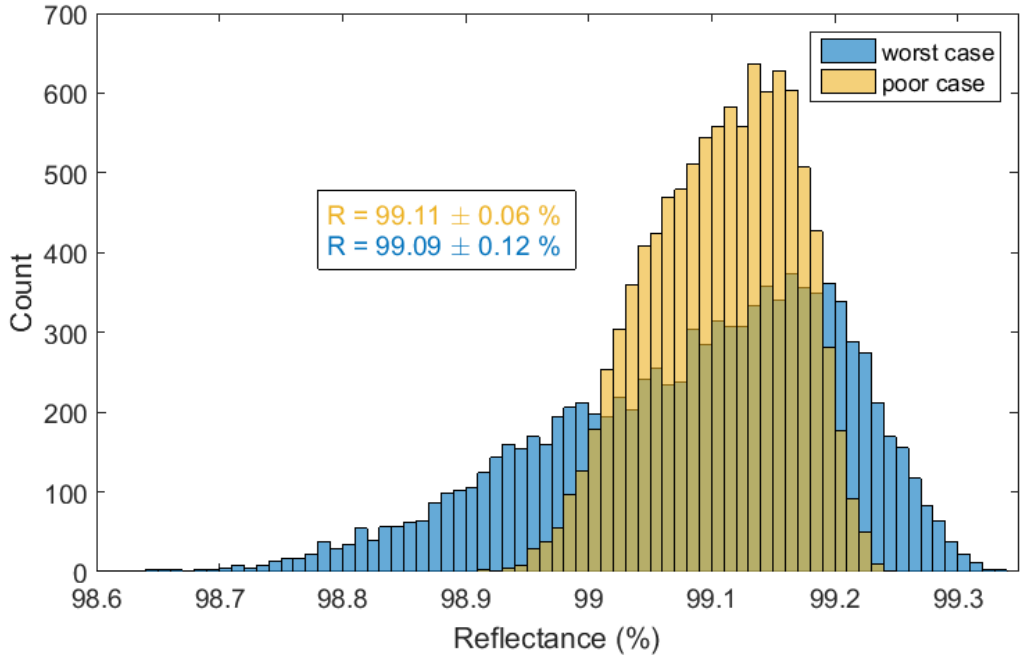

Figure 5.4: *Histograms of poor and worst case simulations for 6-pair SiO_2/a-Si mirrors.*

The poor case results in $R = 99.11 \pm 0.06\%$, whereas a simulation for the same values, but with no variation yields $R = 99.12\%$.

The final results for all of the fabrication reliability simulations performed for 2-8-pair mirrors for both material schemes are presented in Sections 5.3.2 and 5.4.2. They are used as the expected simulated results from deposition (R_{sim}) to compare to the measured values of the deposited mirrors.

5.3 SiO_2/TiO_2 Mirrors

5.3.1 Spectral Reflectance Results

Each mirror was tested using the spectral reflectance technique outlined in Section 3.5 with a gold reference mirror with a reflectance taken to be 98% across the whole spectral range. The measured data is plotted against a simulated spectral reflectance done using the transfer matrix method outlined in Section 2.2.1. The data for n and κ is taken from the ellipsometer data collected when calibrating the sputtering tool prior to the deposition of each DBR. d, the layer thickness, is taken to be ${}^{980\,\mathrm{nm}}/_{4n}$. The ellipsometer only measures up to 1000 nm, so the data beyond that for the simulation is extrapolated by fitting the Cauchy model to the collected ellipsometer data. The calibrated data prior to the deposition is taken as opposed to the averaged data from all calibration runs presented Section 5.2 since the calibrated data just

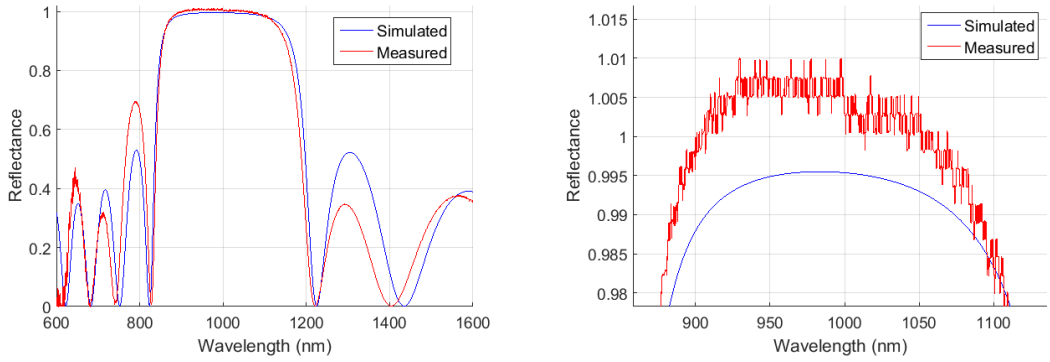

(a) (b)

Figure 5.5: *Spectral reflectance measurement and simulation results for 6-pair SiO_2/TiO_2 mirror for (a) whole measured range, and (b) zoomed-in to stopband.*

prior to the run should be more accurate for that specfic run than the overall averaged results that were collected over months.

An example is provided here for a 6-pair SiO_2/TiO_2 DBR in Figure 5.5, and the remaining SiO_2/TiO_2 DBRs for 2-, 4-, and 8-pair mirrors can be found in Appendix A.1.

The problems with the spectral reflectance technique are highlighted in these results since it is seen the reflectance measured is noisy. In addition, the measured reflectance goes above 100 %, which is not physical, and the reflectance level shifts at 1000 nm where the OSA switches between the detectors used. Because of this shift at 1000 nm, the results near 980 nm show variation up to 1 % meaning it is impossible to measure reflectances above 99 % reliably. Due to these reasons, the spectral reflectance technique is not used to extract absolute reflectances, but is still useful to observe the general shape of the reflectance, and compare with the corresponding simulation to verify the deposition did not go awry.

5.3.2 z-Method Results

One set of raw data, along with the data plotted for extracting the reflectance of a 2-pair SiO_2/TiO_2 DBR will be shown as an example in Table 5.10, and the plotted graphs with extracted R can be found in Figures 5.6a and 5.6b. The 2-pair is chosen since it best shows the non-linear nature of the raw data. A plot of an 8-pair SiO_2/TiO_2 DBR is shown in Figure 5.6c and 5.6d to illustrate how the results change for lower and higher reflectance. The remaining DBRs will be presented with just their measured reflectances.

The final results for the measured reflectances of the deposited SiO_2/TiO_2 DBRs can be seen Figure 5.7 along with the simulated values. The corresponding data is also presented in Table 5.11. The simulated values here use the average results of all the calibration depositions, along with error bars calculated from reliability simulations with these values for each number of pairs. The error bars associated with the measurements were calculated using the method presented in Section 5.1, and the relative detection noise is taken to be the measured detection

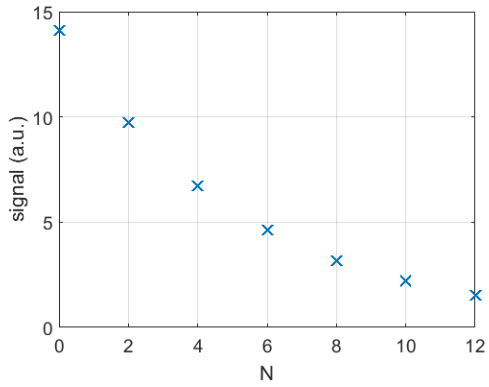

(a) *2-pair raw data*

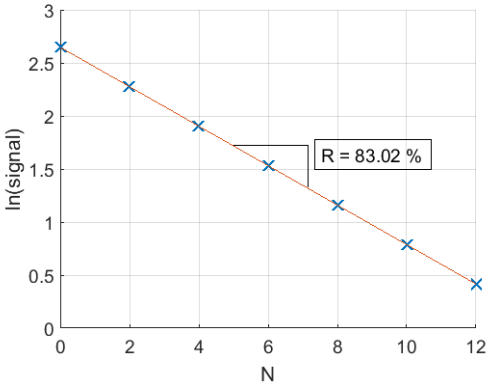

(b) *2-pair data for R extraction*

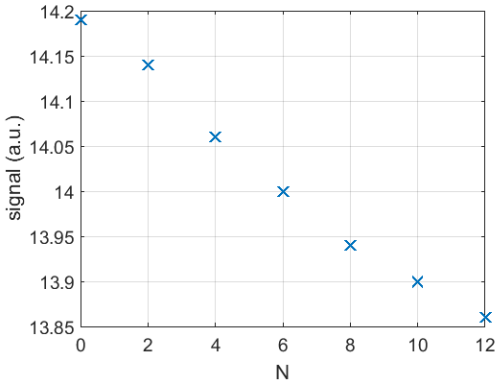

(c) *8-pair raw data*

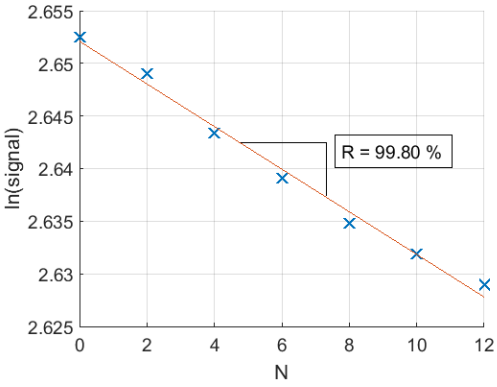

(d) *8-pair data for R extraction*

Figure 5.6: *Measured data and R extraction for 2- and 8-pair SiO_2/TiO_2 mirrors.*

Table 5.10: *Raw signal and ln(signal) data collected from z-method.*

N	signal (a.u.)	ln(signal)
0	14.10	2.6462
2	9.73	2.2752
4	6.71	1.9036
6	4.64	1.5347
8	3.19	1.1600
10	2.20	0.7885
12	1.51	0.4121

Table 5.11: *Reflectance of measured and simulated SiO_2/TiO_2 mirrors.*

DBR Pairs	R_{meas} (%)	R_{sim} (%)
2	83.02 ± 0.13	83.18 ± 0.57
3	-	92.81 ± 0.31
4	97.08 ± 0.04	97.01 ± 0.15
5	-	98.78 ± 0.07
6	99.42 ± 0.03	99.50 ± 0.03
7	-	99.80 ± 0.01
8	99.80 ± 0.03	99.92 ± 0.01

noise of the system over the signal obtained with the maximum of 12 reflections. This corresponds to the lowest signal measured, and gives the largest error bars.

5.3.3 GaAs Incidence

All of the measured results are for a beam incident from air onto the DBR stack on silicon, and the simulations presented so far also reflect this setup. However, the DBRs will ultimately be used in a VCSEL where the light will not be incident from air, but instead from GaAs in the VCSEL cavity. Therefore, simulations to see how this changes the reflectance are important. Again, the average values of the depositions are used. The simulation results for various configurations are presented in Table 5.12 for light at 980 nm. $n(980\,\text{nm})$ for GaAs is taken to be 3.5160 [33].

Table 5.12: *R for 2-, 4-, 6-, and 8-pair mirrors for various configurations of SiO_2/TiO_2 mirrors.*

	$\rightarrow$air/TiO_2/SiO_2/Si	$\rightarrow$GaAs/SiO_2/TiO_2/air	$\rightarrow$GaAs/TiO_2/SiO_2/air
R_{2pair} (%)	83.28	83.02	7.29
R_{4pair} (%)	97.06	97.00	68.59
R_{6pair} (%)	99.51	99.50	94.04
R_{8pair} (%)	99.92	99.92	99.00

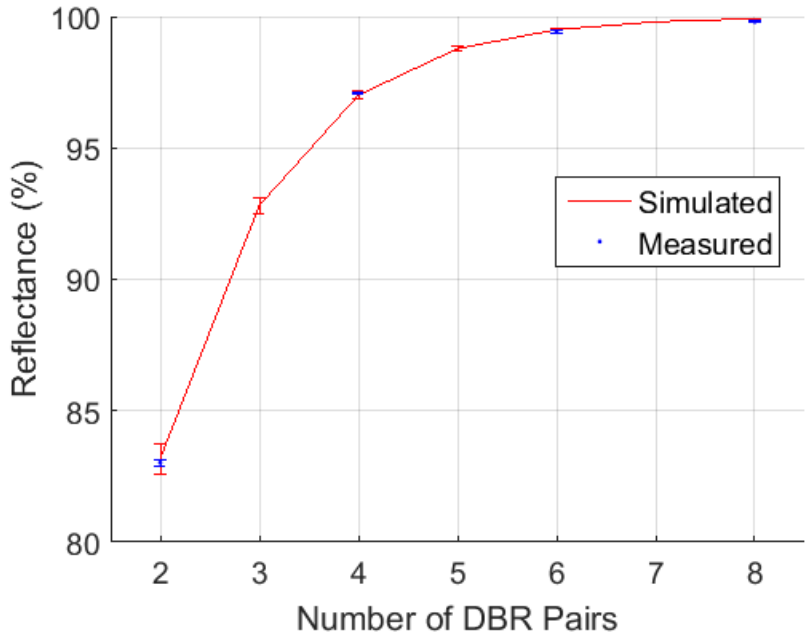

(a)

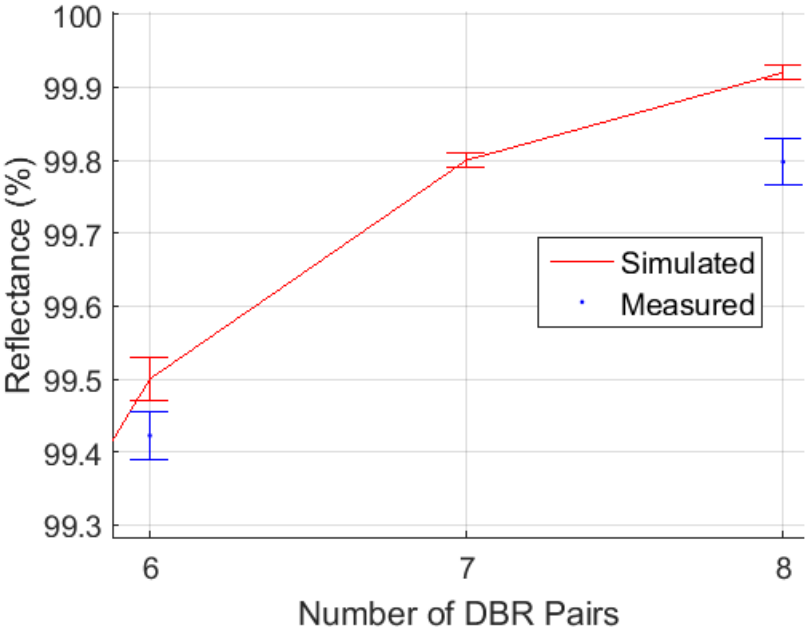

(b)

Figure 5.7: *Measured and simulated R vs. mirror pairs for SiO_2/TiO_2 mirrors for (a) all mirrors, and (b) restricted to 6-8-pairs.*

It is seen that for incidence →air/TiO_2/SiO_2/Si and →GaAs/SiO_2/TiO_2/air the results are almost identical. This is because the first interface is the most important since the highest intensity of light is there. We can calculate R at the first interfaces with

$$R_{air\to TiO_2} = \left[\frac{n_{TiO_2} - n_{air}}{n_{air} + n_{TiO_2}}\right]^2 = \left[\frac{2.2784 - 1}{1 + 2.2784}\right]^2 = 15.21\%,$$
$$R_{GaAs\to SiO_2} = \left[\frac{n_{SiO_2} - n_{GaAs}}{n_{GaAs} + n_{SiO_2}}\right]^2 = \left[\frac{1.4488 - 3.5160}{3.5160 + 1.4488}\right]^2 = 17.34\%,$$
$$R_{GaAs\to TiO_2} = \left[\frac{n_{TiO_2} - n_{GaAs}}{n_{GaAs} + n_{TiO_2}}\right]^2 = \left[\frac{2.2784 - 3.5160}{3.5160 + 2.2784}\right]^2 = 4.56\%.$$

$R_{air\to TiO_2}$ and $R_{GaAs\to SiO_2}$ are very close, so it is expected that these DBRs would also be very close in reflectance which is seen. This is a very nice result since what is measured and what is intended to be incorporated into a VCSEL have very similar reflectances for the DBRs. As a result you can be confident the reflectance you measure with the z-method will be very close to the reflectance of the real VCSEL configuration.

5.4 SiO_2/a-Si Mirrors

5.4.1 Spectral Reflectance Results

As for the case of the SiO_2/TiO_2 mirrors, the simulated spectral reflectance uses data for n_{SiO_2}, n_{a-Si}, and κ_{SiO_2} taken from the ellipsometer data collected when calibrating the sputtering tool prior to the deposition of each DBR. κ for a-Si is taken to 0.015, an empirical fit to the results of the z-method (see following section for how this value was extracted). d is taken to be $^{980\,\mathrm{nm}}/_{4n}$. Again, data for optical properties beyond 1000 nm for the simulation is extrapolated by fitting the Cauchy model to the collected ellipsometer data.

An example is provided here for a 6-pair SiO_2/a-Si DBR in Figure 5.8, and the remaining SiO_2/a-Si DBRs for 2-, 4-, and 8-pair mirrors can be found in Appendix A.2.

The slight discrepancies in where the stopband begins and ends can be explained by variations in n and d of the layers in the deposition of the mirror.

5.4.2 z-Method Results

The final results for the measured reflectances of the deposited SiO_2/a-Si DBRs can be seen Figure 5.9 along with the simulated values. The corresponding data is also presented in Table 5.13. The simulated values here use the average results of all the calibration depositions, along with error bars calculated from reliability simulations with these values for each number of pairs. The 6-pair mirror deposited using an RF power of 1.0 kW is presented along with the four mirrors deposited using an RF power of 0.50 kW. The error bars for the simulated values and measured results are calculated in the same way as for the TiO_2 mirrors.

Note that the 2- and 4-pair mirrors were deposited together, while the 6- and 8-pair mirrors were deposited together. This could explain why they follow different curves for different κ

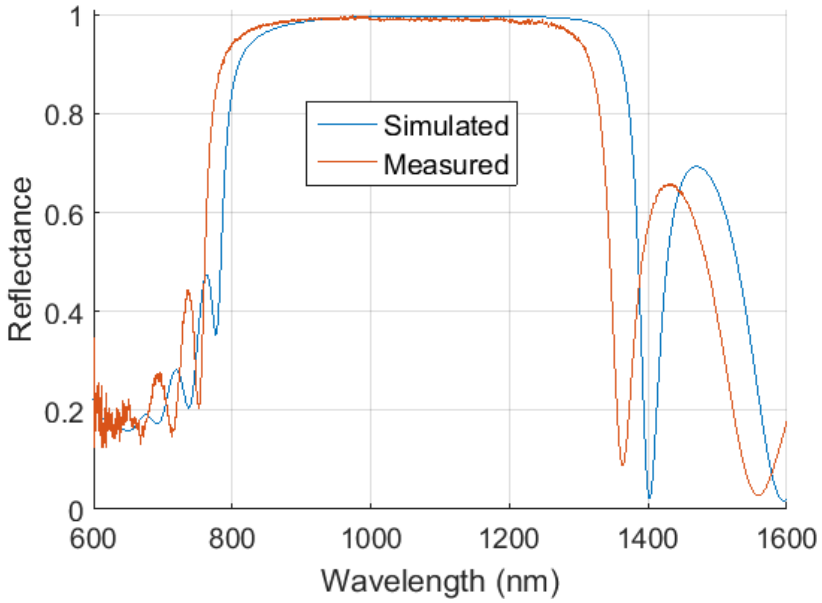

Figure 5.8: *Spectral reflectance measurement and simulation results for 6-pair SiO_2/a-Si mirror.*

Table 5.13: *Reflectance of measured and simulated SiO_2/a-Si mirrors.*

DBR Pairs	R_{meas} (%)	R_{sim} (%) ($\kappa = 0.010$)	R_{sim} (%) ($\kappa = 0.015$)
2	96.45 ± 0.04	96.41 ± 0.28	96.13 ± 0.29
3	-	98.90 ± 0.08	98.61 ± 0.10
4	99.36 ± 0.03	99.32 ± 0.04	99.03 ± 0.06
5	-	99.39 ± 0.04	99.10 ± 0.06
6	99.02 ± 0.03	99.40 ± 0.04	99.11 ± 0.06
(1.0 kW) 6	99.12 ± 0.03		
7	-	99.41 ± 0.04	99.11 ± 0.06
8	99.17 ± 0.03	99.41 ± 0.04	99.11 ± 0.06

values. The extinction coefficient was fit to this data separately for 2- and 4-pairs and 6- and 8-pairs. Interestingly, the mirror deposited using higher RF power matches closely with the equivalent mirror deposited using the lower RF power. This could be just a coincidence that the different trials yielded very similar results for 6-pair mirrors. Another explanation is temperature influencing the film deposition, since sputtered a-Si is known to be heavily influenced by temperature. The RF power used when sputtering SiO_2 and a-Si heats up the substrate, and when depositing more layers, the substrate can heat up drastically. This could explain the results seen that less pairs (shorter overall deposition time) have different optical properties than mirrors with more pairs. If the extinction coefficient increases for layers deposited at higher temperatures, then we would expect to obtain the results that were

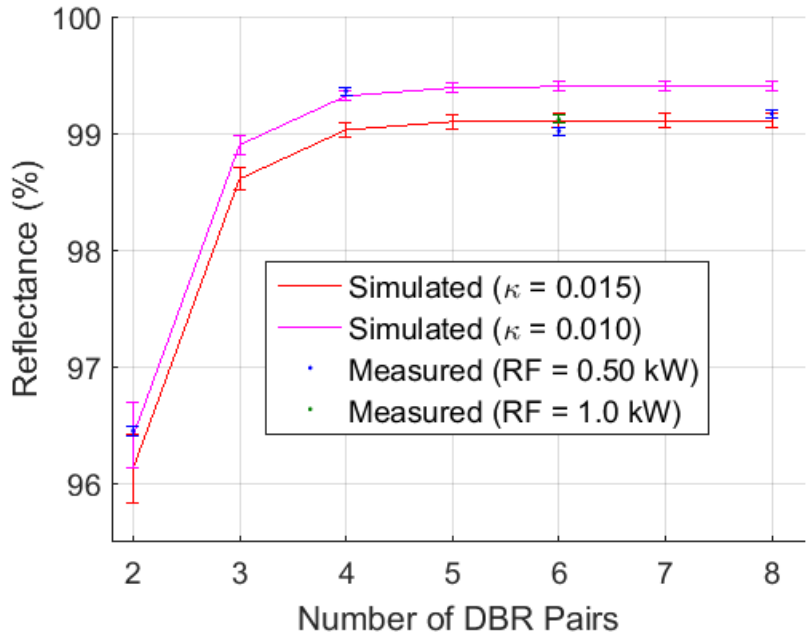

(a)

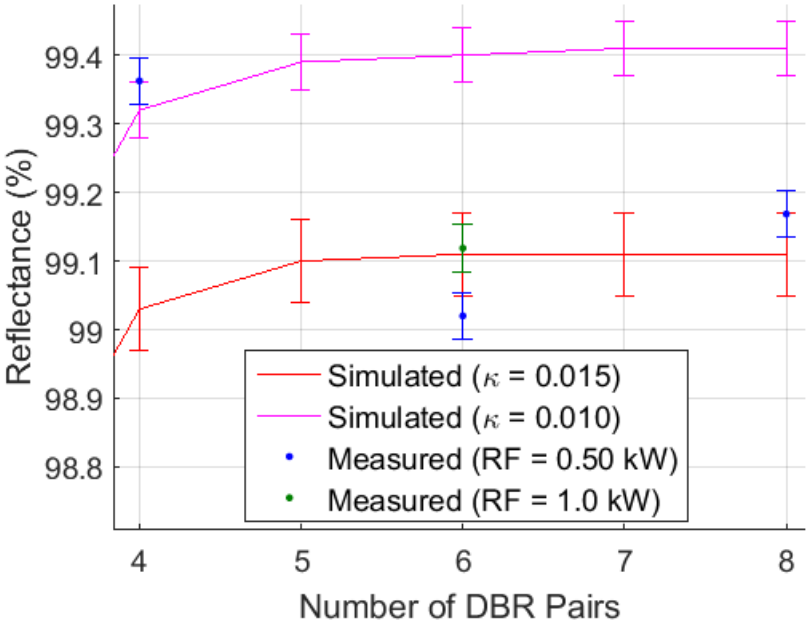

(b)

Figure 5.9: *Measured and simulated R vs. mirror pairs for SiO_2/a-Si mirrors for (a) all mirrors, and (b) restricted to 4-8-pairs.*

measured. The a-Si layers deposited with higher temperature are closer to the surface, so when they are measured using the z-method the strongest optical field would be in these layers that absorb more. The a-Si layers closer to the substrate would still have the lower extinction coefficient, but less light is in these layers so the effect is that the top layers with higher κ dominate the results. More investigation is required to understand if this is the case, or if it was due to other deposition parameters. An alternate explanation following the same vein is that more stress in the layers causes a higher extinction coefficient. This is also a plausible explanation since it was found that stress builds up as more pairs of SiO_2/a-Si are added. An exploration for deposition parameters that reduce stress in a-Si could be of interest. Regardless, the deposition parameters need to optimized for a-Si since $\kappa = 0.010$ is too high to be used as a top mirror in a VCSEL DBR and the deposition results show too much variance between depositions to be used reliably.

Instead of using pure a-Si, hydrogenated a-Si can be used instead to improve the extinction coefficient. Pure a-Si can suffer from dangling bonds which increase absorption for near-infrared wavelengths. To counteract this, hydrogen can be incorporated to saturate the dangling bonds and lower the optical losses [49]. This is another avenue worth exploring to improve the SiO_2/a-Si DBRs, however a different deposition technique would need to be used to incorporate the hydrogen, such as plasma enhanced chemical vapour deposition.

The extracted extinction coefficients can be converted to an absorption coefficient, α, by

$$\alpha = \frac{4\pi\kappa}{\lambda_0}, \tag{5.1}$$

which gives $\alpha(\kappa = 0.010) = 1282\,\mathrm{cm}^{-1}$ and $\alpha(\kappa = 0.015) = 1923\,\mathrm{cm}^{-1}$ for 980 nm. For hydrogenated a-Si, a much lower absorption coefficient of $\alpha = 115\,\mathrm{cm}^{-1}$ is reported at $1.5\,\mu$m [50].

5.4.3 GaAs Incidence

Again, the DBRs will ultimately be used in a VCSEL where the light will be incident from GaAs in the VCSEL cavity. The average values of the depositions are used, and $\kappa(980\,\mathrm{nm})$ was set to 0.015. The simulation results for various configurations are presented in Table 5.14 for light at 980 nm.

Table 5.14: *R for 2-, 4-, 6-, and 8-pair mirrors for various configurations of SiO_2/a-Si mirrors.*

	→air/a-Si/SiO_2/Si	→GaAs/SiO_2/a-Si/air	→GaAs/a-Si/SiO_2/air
R_{2pair} (%)	96.19	96.47	66.29
R_{4pair} (%)	99.04	99.39	95.95
R_{6pair} (%)	99.12	99.47	96.91
R_{8pair} (%)	99.12	99.47	96.94

It is seen that for incidence →air/a-Si/SiO_2/Si and →GaAs/SiO_2/a-Si/air the results are similar, but incidence from GaAs to SiO_2 is better. We can again calculate R at the first interfaces to see how this might affect the results

$$R_{air\to a-Si} = \left[\frac{n_{a-Si} - n_{air}}{n_{air} + n_{a-Si}}\right]^2 = \left[\frac{3.5705 - 1}{1 + 3.5705}\right]^2 = 31.63\%,$$

$$R_{GaAs\to SiO_2} = \left[\frac{n_{SiO_2} - n_{GaAs}}{n_{GaAs} + n_{SiO_2}}\right]^2 = \left[\frac{1.4488 - 3.5160}{3.5160 + 1.4488}\right]^2 = 17.34\%,$$

$$R_{GaAs\to a-Si} = \left[\frac{n_{a-Si} - n_{GaAs}}{n_{GaAs} + n_{a-Si}}\right]^2 = \left[\frac{3.5705 - 3.5160}{3.5160 + 3.5705}\right]^2 = 0.01\%.$$

Here we actually see some interesting results. For example, GaAs → a-Si essentially removes a half-pair from the DBR since the refractive index contrast is almost zero. In addition, air → a-Si has the highest reflectance, but does not yield the best mirrors. This is because although it reflects the most, it also transmits the most light into absorbing a-Si layers since the a-Si layer is first. For the GaAs → SiO_2 mirror, there are two interfaces for reflection before the light enters the first absorbing layer, so in the end this mirror scheme wins out even though it has poorer reflectance at the first interface since less light reaches the absorbing a-Si layers. The measurement setup yields reflectance values a bit lower than what would be used in a VCSEL. This means that for this set of mirrors the measured value will serve as a lower bound on the actual reflectance in a VCSEL.

The results also show that the reflectance saturates past 6-pairs. The saturation of the a-Si mirrors means that they are not useful for a top reflector in a VCSEL since the light that is not reflected is being absorbed. This means that there is no light transmitted out of the laser, so it not a useable device. An a-Si DBR could be used as a bottom mirror, but as explained previously this increases the fabrication complexity since heat spreading layers need to be added to remove heat from the laser's cavity. These a-Si mirrors could also be used in a hybrid-cavity vertical-cavity laser where light is tapped out the side of the laser using a diffraction grating or high-contrast grating instead of surface emission. This configuration is useful for integration with silicon photonics where light can be tapped out the side into waveguides [18].

5.5 TiO_2 vs. a-Si Discussion

While a-Si offers superior refractive index contrast with SiO_2 and therefore has the ability to offer higher reflectances than TiO_2, at present TiO_2 appears to be the better path forward. Both materials were able to achieve the required reflectance of $>99\%$ reflectance required for VCSELs, however TiO_2 was able to achieve higher reflectances, while the a-Si reflectance saturated after 6-pairs at around 99.2 %. TiO_2 on the other hand showed no saturation up to 8-pairs, meaning there is light being transmitted out, so a useable VCSEL can be fabricated.

Not only was the reflectance better for the TiO_2 mirrors, but also the fabrication results are more reliable. Over the course of the work, TiO_2 showed less variation in both refractive index and deposition rate for sputtered layers than a-Si. This means what is expected to be deposited will actually be deposited, and the results are less susceptible to random process variations. This is key to fabrication since as much control and reliability as possible is needed throughout the process to get a favourable yield of working devices in the end.

There are some benefits to a-Si however which make it interesting for continued research in this topic. If deposition parameters can be fine tuned, it can be deposited much quicker than TiO_2, can achieve an extinction coefficient to match TiO_2, offers higher refractive index contrast, and can be etched easier.

At present, a 6-pair SiO_2/TiO_2 DBR appears to be the best for making VCSELs with a top dielectric DBR. This was found to have $R = 99.42 \pm 0.03\,\%$, exceeding the threshold reflectance for lasing in a VCSEL. The 6-pair is preferred over the 8-pair since it has a slightly lower reflectance, which means that is has more transmitted light, achieving higher output powers.

Chapter 6

Conclusion

The goal of the thesis was to deposit DBRs with reflectance above 99 % using sputtering to improve the performance of VCSELs operating at 980 nm. Different material choices and number of pairs were evaluated to achieve this.

Thin-films of SiO_2, TiO_2, and a-Si were sputtered on silicon substrates, and their optical properties were measured using ellipsometry. Over many depositions, the refractive indices were found to be 1.4488 ± 0.0047, 2.2784 ± 0.0179, and 3.5705 ± 0.1542 for SiO_2, TiO_2, and a-Si respectively. Their deposition rates were found to be 0.2283 ± 0.0053 nm/s, 0.1278 ± 0.0017 nm/s, and 0.2139 ± 0.0070 nm/s respectively.

These values were used to perform simulations on the reliability of the sputtering parameters to deposit DBRs at 980 nm. For 6-pair DBRs, it was found that a reflectance of 99.50 ± 0.03 % could be expected for SiO_2/TiO_2 DBRs, and 99.11 ± 0.06 % could be expected for SiO_2/a-Si DBRs. These simulations were done using the transfer matrix method.

A measurement setup was built based on the z-method to measure the absolute reflectance of deposited DBRs. This was required since DBRs for VCSELs require >99 % reflectance, and the existing reflectance measurement setup could only measure to within 1 %. This would make comparing DBRs with reflectance above 99 % impossible. This method was found to be able to measure reflectances above 99 % with an accuracy of ± 0.03 %.

DBRs were deposited with 2, 4, 6, and 8 pairs for both SiO_2/TiO_2 and SiO_2/a-Si mirrors designed for 980 nm incident light, and measured with the z-method setup. Reflectances above 99 % were achieved for 6-pair and 8-pair SiO_2/TiO_2 mirrors with values of 99.42 ± 0.03 % and 99.80 ± 0.03 % respectively. These compared well to the simulated results, but were ultimately a little bit lower. Reflectances above 99 % were achieved for 4-, 6-, and 8-pair SiO_2/a-Si mirrors with values of 99.36 ± 0.03 %, 99.02 ± 0.03 %, and 99.17 ± 0.03 % respectively. Simulation results indicate that these values correspond to an extinction coefficient between 0.0010 and 0.0015 (absorption coefficient between 1282 cm^{-1} and 1923 cm^{-1}) for the a-Si layers. The reflectance of SiO_2/a-Si was found to saturate around 99.2 %, indicating that little to no light would be transmitted out of these DBRs, diminishing their usefulness for the top mirror in a VCSEL.

Simulations were also performed to see how the reflectance of the deposited DBRs would be affected for incidence from GaAs, since this is the configuration that would be used in a real VCSEL. For SiO_2/TiO_2 mirrors, the reflectance was found to be almost identical since

the refractive index contrast of air/TiO_2 is almost identical to that of GaAs/SiO_2. For the case SiO_2/a-Si mirrors, switching to GaAs incidence was found to increase the reflectance from 99.12 % to 99.47 % even though air/a-Si has a higher refractive index contrast than GaAs/SiO_2. This was because the first absorbing a-Si layer would be moved further from the incident light in this configuration. Again the reflectance was found to saturate for GaAs incidence as well.

In the end, SiO_2/TiO_2 mirrors with 6-pairs were chosen to be the best option for 980 nm VCSELs for a number of reasons. The reliability of these materials is superior, and there was no absorption measured for these materials. 6-pairs was chosen over 8-pairs since the slightly lower reflectance means there is more output power from the VCSEL, while still maintaining >99 % reflectance reliably.

Nonetheless, a-Si is still a very interesting material to continue exploring in future work since it has higher refractive index contrast, and can theoretically be deposited under the right conditions to achieve an extinction coefficient near zero at 980 nm. It also provides easier integration into existing fabrication schemes than TiO_2.

Appendix A

Spectral Reflectance Data

This appendix contains the plots for measured spectral reflectance along with their corresponding simulated results for mirrors deposited with 2, 4, 6, and 8 pairs for both SiO_2/TiO_2 and SiO_2/a-Si.

A.1 SiO_2/TiO_2 Mirrors

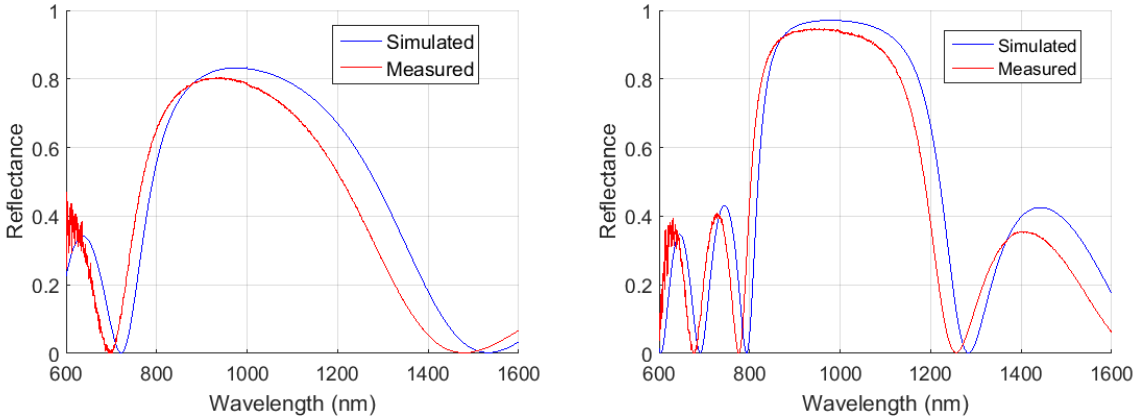

(a) *2 pairs*

(b) *4 pairs*

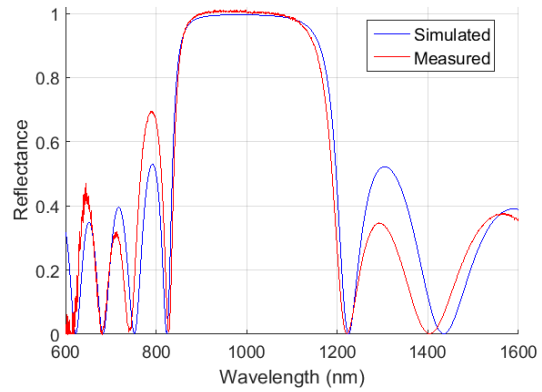

(c) *6 pairs*

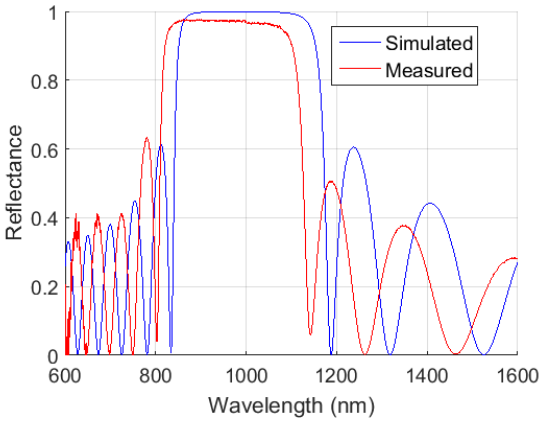

(d) *8 pairs*

Figure A.1: *Measured spectral reflectance and corresponding simulated results for SiO_2/TiO_2 mirrors.*

A.2 SiO_2/a-Si Mirrors

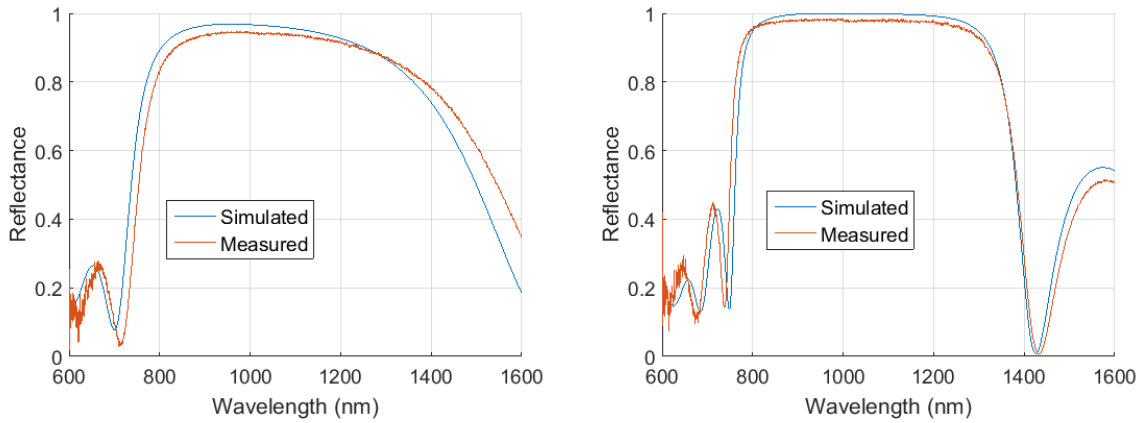

(a) *2 pairs*

(b) *4 pairs*

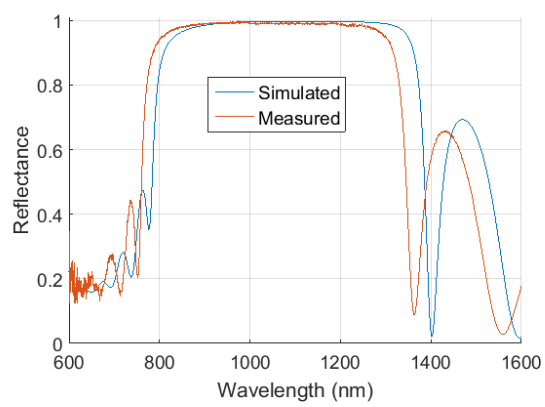

(c) *6 pairs*

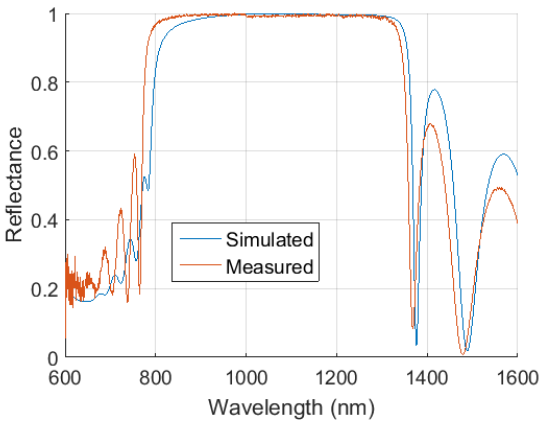

(d) *8 pairs*

Figure A.2: *Measured spectral reflectance and corresponding simulated results for SiO_2/a-Si mirrors.*

References

[1] Christoforos Kachris and Ioannis Tomkos. 'A survey on optical interconnects for data centers'. In: *Communications Surveys & Tutorials, IEEE* 14.4 (2012), pp. 1021–1036.

[2] Petter Westbergh et al. 'High-speed 850 nm VCSELs operating error free up to 57 Gbit/s'. In: *Electronics Letters* 49.16 (2013), p. 1.

[3] Daniel M Kuchta et al. 'A 71-Gb/s NRZ Modulated 850-nm VCSEL-Based Optical Link'. In: *IEEE PHOTONICS TECHNOLOGY LETTERS* 27.6 (2015), p. 577.

[4] Anders Larsson. 'Advances in VCSELs for communication and sensing'. In: *IEEE Journal of Selected Topics in Quantum Electronics* 6.17 (2011), pp. 1552–1567.

[5] R. I. Laming et al. 'Efficient pump wavelengths of erbium-doped fibre optical amplifier'. In: *Electronics Letters* 25.1 (Jan. 1989), pp. 12–14.

[6] B. Mukherjee. 'WDM optical communication networks: progress and challenges'. In: *IEEE Journal on Selected Areas in Communications* 18.10 (Oct. 2000), pp. 1810–1824.

[7] R. J. Mears et al. 'Low-noise erbium-doped fibre amplifier operating at 1.54 um'. In: *Electronics Letters* 23.19 (Sept. 1987), pp. 1026–1028.

[8] Alex Mutig and Dieter Bimberg. 'Progress on high-speed 980 nm VCSELs for short-reach optical interconnects'. In: *Advances in Optical Technologies* 2011 (2011).

[9] Larry A Coldren et al. 'Efficient sources for chip-to-chip to box-to-box communication within data centers'. In: *IEEE Summer Topicals* (2010).

[10] Kenichi Iga, Fumio Koyama and Susumu Kinoshita. 'Surface emitting semiconductor lasers'. In: *Quantum Electronics, IEEE Journal of* 24.9 (1988), pp. 1845–1855.

[11] TH Maiman. 'Stimulated Optical Radiation in Ruby'. In: *Nature* 187.4736 (1960), pp. 493–494.

[12] Robert N Hall et al. 'Coherent light emission from GaAs junctions'. In: *Physical Review Letters* 9.9 (1962), p. 366.

[13] Kenichi Iga. 'Surface-emitting laser-its birth and generation of new optoelectronics field'. In: *Selected Topics in Quantum Electronics, IEEE Journal of* 6.6 (2000), pp. 1201–1215.

[14] Haruhisa Soda et al. 'GaInAsP/InP surface emitting injection lasers'. In: *Japanese Journal of Applied Physics* 18.12 (1979), p. 2329.

[15] Jack L Jewell et al. 'Vertical-cavity surface-emitting lasers: design, growth, fabrication, characterization'. In: *IEEE Journal of Quantum Electronics* 27.6 (1991), pp. 1332–1346.

[16] Philip Moser et al. 'Error-free 46 Gbit/s operation of oxide-confined 980 nm VCSELs at 85 C'. In: *Electronics Letters* 50.19 (2014), pp. 1369–1371.

[17] Philip Wolf et al. 'High-speed and temperature-stable, oxide-confined 980-nm VCSELs for optical interconnects'. In: *Selected Topics in Quantum Electronics, IEEE Journal of* 19.4 (2013), pp. 1701207–1701207.
[18] Emanuel P Haglund et al. 'Silicon-integrated short-wavelength hybrid-cavity VCSEL'. In: *Optics Express* 23.26 (2015), pp. 33634–33640.
[19] Silvia Spiga et al. 'Single-Mode 1.5-μm VCSELs with 22-GHz Small-Signal Bandwidth'. In: *Optical Fiber Communication Conference*. Optical Society of America. 2016, Tu3D–4.
[20] Eugene Hecht. *Optics, fourth edition*. Addison-Wesley, 2001.
[21] H Angus Macleod. *Thin-film optical filters*. CRC press, 2001.
[22] Larry A Coldren, Scott W Corzine and Milan L Mashanovitch. *Diode lasers and photonic integrated circuits*. John Wiley & Sons, 2012.
[23] Milton Ohring. *Materials science of thin films*. Academic press, 2001.
[24] JT Leonard et al. 'Smooth e-beam-deposited tin-doped indium oxide for III-nitride vertical-cavity surface-emitting laser intracavity contacts'. In: *Journal of Applied Physics* 118.14 (2015), p. 145304.
[25] *Guide to Using WVASE32*. J. A. Woollam Co., Inc., 2010.
[26] Franz Urbach. 'The long-wavelength edge of photographic sensitivity and of the electronic absorption of solids'. In: *Physical Review* 92.5 (1953), p. 1324.
[27] Hitoshi Sumi and Yutaka Toyozawa. 'Urbach-Martienssen rule and exciton trapped momentarily by lattice vibrations'. In: *Journal of the Physical Society of Japan* 31.2 (1971), pp. 342–358.
[28] *KLA-Tencor P-15 User's Guide*. KLA-Tencor, 2002.
[29] Matthew A Hopcroft, William D Nix and Thomas W Kenny. 'What is the Young's Modulus of Silicon?' In: *Microelectromechanical Systems, Journal of* 19.2 (2010), pp. 229–238.
[30] Claude-Albert Berseth et al. 'Experimental method for high-accuracy reflectivity-spectrum measurements'. In: *Applied optics* 37.28 (1998), pp. 6671–6676.
[31] *Si photodiodes S2281 series*. Hamamatsu, 2015.
[32] *Model 5209 Single Phase Lock-in Amplifier Instruction Manual*. Ametek Advanced Measurement Technology, Inc., 2002.
[33] T Skauli et al. 'Improved dispersion relations for GaAs and applications to nonlinear optics'. In: *Journal of Applied Physics* 94.10 (2003), pp. 6447–6455.
[34] RE Fern and A Onton. 'Refractive index of AlAs'. In: *Journal of applied physics* 42.9 (1971), pp. 3499–3500.
[35] Lihong Gao, Fabien Lemarchand and Michel Lequime. 'Exploitation of multiple incidences spectrometric measurements for thin film reverse engineering'. In: *Optics express* 20.14 (2012), pp. 15734–15751.
[36] J Rs DeVore. 'Refractive indices of rutile and sphalerite'. In: *JOSA* 41.6 (1951), pp. 416–419.
[37] C Asplund et al. 'Doping-induced losses in AlAs/GaAs distributed Bragg reflectors'. In: *Journal of Applied Physics* 90.2 (2001), pp. 794–800.
[38] DT Pierce and WE Spicer. 'Electronic structure of amorphous Si from photoemission and optical studies'. In: *Physical Review B* 5.8 (1972), p. 3017.

[39] Jan Kischkat et al. 'Mid-infrared optical properties of thin films of aluminum oxide, titanium dioxide, silicon dioxide, aluminum nitride, and silicon nitride'. In: *Applied optics* 51.28 (2012), pp. 6789–6798.
[40] Darwin L Wood et al. 'Optical properties of cubic hafnia stabilized with yttria'. In: *Applied optics* 29.4 (1990), pp. 604–607.
[41] TJ Bright et al. 'Infrared optical properties of amorphous and nanocrystalline Ta2O5 thin films'. In: *Journal of Applied Physics* 114.8 (2013), p. 083515.
[42] Stanley R Williams. 'How we found the missing memristor'. In: *Spectrum, IEEE* 45.12 (2008), pp. 28–35.
[43] Benjamin Kögel et al. 'Integrated MEMS-tunable VCSELs using a self-aligned reflow process'. In: *Quantum Electronics, IEEE Journal of* 48.2 (2012), pp. 144–152.
[44] G Dang et al. 'Comparison of dry and wet etch processes for patterning SiO2/TiO2 distributed Bragg reflectors for vertical-cavity surface-emitting lasers'. In: *Journal of The Electrochemical Society* 148.2 (2001), G25–G28.
[45] Martin A Green. 'Crystalline and thin-film silicon solar cells: state of the art and future potential'. In: *Solar energy* 74.3 (2003), pp. 181–192.
[46] Cherie R Kagan and Paul Andry. *Thin-film transistors*. CRC Press, 2003.
[47] Aqing Chen, Qianmin Yuan and Kaigui Zhu. 'ZnO/a-Si distributed Bragg reflectors for light trapping in thin film solar cells from visible to infrared range'. In: *Applied Surface Science* 360 (2016), pp. 693–697.
[48] S Abdesselem et al. 'Growth mechanism of sputtered amorphous silicon thin films'. In: *Physica B: Condensed Matter* 373.1 (2006), pp. 33–41.
[49] Shankar Kumar Selvaraja et al. 'Low-loss amorphous silicon-on-insulator technology for photonic integrated circuitry'. In: *Optics Communications* 282.9 (2009), pp. 1767–1770.
[50] MJA De Dood et al. 'Amorphous silicon waveguides for microphotonics'. In: *Journal of applied physics* 92.2 (2002), pp. 649–653.